International Journal of Thermal Sciences 115 (2017) 176–196

Contents lists available at ScienceDirect

International Journal of Thermal Sciences

journal homepage: www.elsevier.com/locate/ijts

Experimental study on laminar flow over two confined isothermal cylinders in tandem during mixed convection

E. Salcedo [a], C. Treviño [b], C. Palacios-Morales [c], R. Zenit [d], L. Martínez-Suástegui [e, *]

[a] Departamento de Termofluidos, Facultad de Ingeniería, Universidad Nacional Autónoma de México, Av. Universidad 3000, México, Ciudad de México 04510, Mexico
[b] UMDI, Facultad de Ciencias, Universidad Nacional Autónoma de México, Sisal, Yucatán, Mexico
[c] Facultad de Ingeniería, Universidad Nacional Autónoma de México, México, Ciudad de México 04510, Mexico
[d] Instituto de Investigaciones en Materiales, Universidad Nacional Autónoma de México, México, Ciudad de México 04510, Mexico
[e] ESIME Azcapotzalco, Instituto Politécnico Nacional, Avenida de las Granjas No. 682, Colonia Santa Catarina, Delegación Azcapotzalco, México, Ciudad de México 02250, Mexico

ARTICLE INFO

Article history:
Received 16 June 2016
Received in revised form
9 January 2017
Accepted 10 January 2017
Available online 17 February 2017

Keywords:
Tandem cylinders
Vortex shedding
Blockage ratio
Interference effects
PIV
Wall effects

ABSTRACT

An experimental investigation of laminar aiding and opposing mixed convection is carried out using particle image velocimetry (PIV) to assess the thermal effects on the wake of two isothermal cylinders of equal diameter in tandem array placed horizontally and confined inside a vertical closed-loop downward rectangular water channel. The buoyancy effect on the flow distributions are revealed for flow conditions with Reynolds number based on cylinder diameter of $Re = 100$ and 200, blockage ratio of $BR = D/H = 0.3$, aspect ratio of $AR = W/D = 5$, pitch-to-diameter ratio of $\sigma = L/D = 3$, and values of the buoyancy parameter (Richardson number) in the range $-1 \leq Ri \leq 3$. In this work, the interference effects on the complex flow features are presented in the form of mean and instantaneous contours of velocity and vorticity. In addition, separation angles, wake structure, recirculation bubble lengths, time traces of velocity fluctuation, Strouhal number and vortex shedding modes of the two-cylinder system are obtained as a function of the Richardson number. In this arrangement, the results indicate that the effects of the Reynolds number are very pronounced, and that the vortex shedding patterns exhibit a strong dependence on *Ri*. We also show the modulation effect of the channel walls on the three-dimensional flow under varying thermal buoyancy, and the results reported herein demonstrate how the flow structure, wake behavior and vortex shedding pattern are entirely different from that behind a single circular cylinder under wall confinement and thermal effects.

1. Introduction

Vortex shedding associated with the flow past two cylinders in tandem has been extensively studied because of its remarkable complex flow configurations and wide engineering applications in the design of heat exchanger tubes, electronic packages, cooling towers, cooling systems for nuclear fuel rods, offshore structures, seabed pipelines and chimney stacks. Useful reviews on how the interference effects between the cylinders affects the flow structure, wakes, shear layers and fluctuating fluid forces can be found in Refs. [1–6], and multiple investigations have provided important insight into various features of the tandem cylinder system [7–10]. In particular, for two cylinders of equal diameter, the flow structure is sensitive to the Reynolds number and the pitch ratio ($\sigma = L/D$, ratio between the center-to-center pitch and the cylinder diameter), and three basic interference flow regimes between cylinders have been identified depending on how the wake of the upstream cylinder modifies the incoming flow condition of the downstream cylinder: (i) the "extended body" regime occurs for small pitch ratios of approximately $1 < \sigma < 2$. In this regime, the two cylinders behave as a single bluff body and the shear layers that emanate from the upstream cylinder roll-up behind the downstream cylinder and form a single wake [11–15]; (ii) the "reattachment" regime occurs for intermediate pitch ratios of approximately $2 < \sigma < 5$, and two basic flow configurations have been identified depending on whether the location of the shear layer reattachment takes place at the leading surface ("fore-body", $\sigma = 3$–5) or rear ("after-body",

* Corresponding author.
E-mail address: lamartinezs@ipn.mx (L. Martínez-Suástegui).

http://dx.doi.org/10.1016/j.ijthermalsci.2017.01.015
1290-0729/

Nomenclature

AR	cylinder aspect ratio, W/D
BR	blockage ratio, D/H
D	diameter of cylinders (characteristic length)
f	vortex shedding frequency (Hertz)
g	gravity acceleration
Gr	Grashof number based on cylinder diameter, $Gr = g\beta(T_w - T_0)D^3/\nu^2$
H	channel width
k	thermal conductivity of fluid
L_{tot}	total channel length
Pr	Prandtl number, $Pr = \nu/\alpha$
Re	Reynolds number based on cylinder diameter, $Re = u_0 D/\nu$
Ri	Richardson number based on cylinder diameter, $Ri = Gr/Re^2$
L	pitch (center-to-center distance between two cylinders)
SD	standard deviation
St	Strouhal number based on cylinder diameter, $St = fD/u_0$
t	time
T	temperature
T_0	fluid temperature at the channel inlet
T_w	temperature of the surface of the cylinders
u_0	fluid velocity at the channel inlet
u, v	longitudinal and transverse velocity components, respectively
U	nondimensional longitudinal velocity component, $U = u/u_0$
V	nondimensional transverse velocity component, $V = v/u_0$
W	cylinder span (channel depth)
x, y, z	rectangular Cartesian coordinates
X	nondimensional longitudinal coordinate, $X = x/D$
Y	nondimensional transverse coordinate, $Y = y/D$
Z	nondimensional coordinate, $Z = z/D$

Greek symbols

α	thermal diffusivity of fluid
β	volumetric expansion coefficient
ρ	fluid density
ν	kinematic viscosity
ψ	nondimensional stream function
Ω	nondimensional instantaneous out of plane vorticity
σ	nondimensional pitch-to-diameter ratio, $\sigma = L/D$
σ_{v1}	nondimensional wake closure length, $\sigma_{v1} = L_{v1}/D$
σ_{v2}	nondimensional wake closure length, $\sigma_{v2} = L_{v2}/D$
τ	nondimensional time
θ_s	separation angle

Subscripts

0	ambient or reference
1,2	refers to the upstream and downstream cylinder, respectively
w	at the surface of the cylinders

$\sigma = 2$–3) of the downstream cylinder [16–20]; and (iii) the co-shedding regime takes place at higher pitch ratios of approximately $\sigma > 5$. In this regime, a vortex street forms behind each cylinder and the vortex shedding from both cylinders takes place at the same frequency [21,22]. In spite that investigations of flow past a circular cylinder placed in a plane channel show that the blockage effect has a significant influence on the flow pattern, force coefficients, length of the recirculation zone, separation angle and Strouhal number, the great majority of research has been made for unconfined cylinder arrays [23–26], and only few comprehensive flow and heat transfer studies have been conducted to assess the confinement effect [27–30].

The foregoing survey of literature reveals that although the interest in heat transfer from tandem cylinders in cross-flow has grown in the last decades, the majority of the contributions to the scientific literature consider the natural [31–45] or forced convection regime [46–56], and limited research has been conducted regarding the effect of blockage constraints under varying thermal buoyancy [57–59]. The main goal of the present study is to perform an experimental investigation using PIV to characterize the flow patterns around two stationary isothermal circular cylinders of equal diameter in tandem arrangement under assisting/opposing buoyancy conditions subjected to a steady cross-flow and wall proximity effects. Two-dimensional spatio-temporal measurements of velocity and vorticity in parallel and perpendicular planes with respect to the span of the cylinders are made in order to gain a better insight of the dynamic interaction between the boundary layers, separating shear layers and the unsteady wakes. Flow visualization images are presented to support the PIV data.

The paper is organised as follows. In Section 2, we describe the experimental setup and provide details about image acquisition, data processing and the uncertainty analysis. Results for the mean

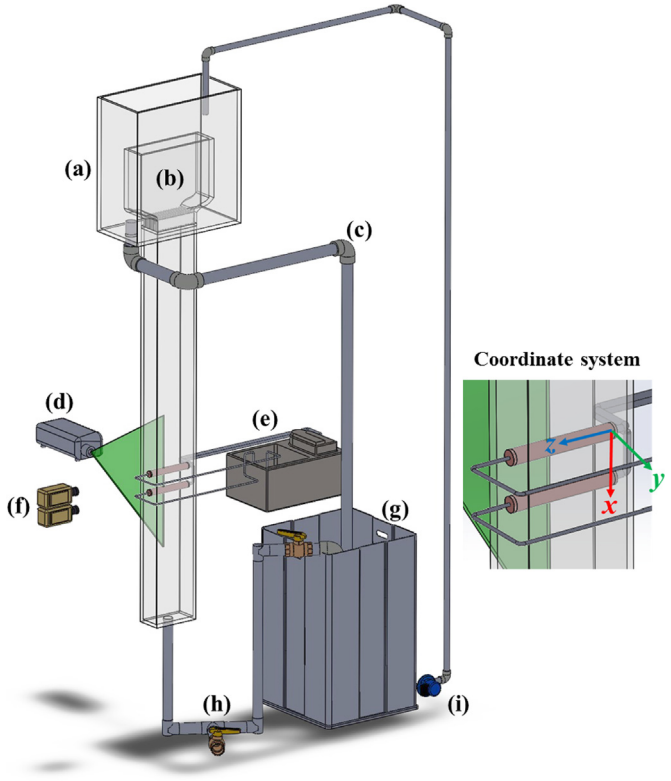

Fig. 1. Schematic diagram of the experimental setup. (a) Constant head tank. (b) Nozzle section with honeycomb and mesh structures. (c) Overflow tube. (d) Laser. (e) Constant-temperature refrigerated bath. (f) CMOS digital cameras. (g) Storage tank. (h) Adjustable valve. (i) Centrifugal pump.

and instantaneous flow distributions and overall response characteristics of the cylinder system are presented and discussed at Section 3. Finally, Section 4 summarises the main findings of this work.

2. Materials and methods

2.1. Experimental setup

Fig. 1 shows a schematic diagram of the experimental set-up used for the present study. A 3D Cartesian coordinate system with its origin located at the center point of the upstream cylinder is selected, such that the x, y and z-axes are set along the streamwise, transverse and spanwise directions, respectively. The cylinders are exposed to a vertical uniform cross-flow, and experiments are carried out under hydrodynamic developing flow conditions. Water enters through the upper opening of a gravity-driven vertical rectangular duct of width $H = 95.7$ mm, depth $W = 143.5$ mm and 1.82 m long with a uniform velocity u_0 and temperature T_0. The channel walls are made of transparent 9 mm thick Plexiglas ($k \approx 0.189$ W/m K) and they are at free stream temperature T_0. Exposed to a cross-flow, two copper tubes of diameter $D = 28.7$ mm are placed horizontally and symmetrically bounded by two parallel end walls of the test section. Both cylinders have the same aspect ratio (AR, ratio between the length and diameter of the cylinder) of 5, the blockage ratio (BR, ratio between the cylinder diameter and the thickness of rectangular section) is of 0.3, and the nondimensional center-to-center distance between the cylinder axes is $\sigma = 3$. The surface temperature T_w of both cylinders is maintained uniform and constant from outside by internally circulating the water inside the tubes in a closed loop that is connected to a constant-temperature refrigerated bath (TECHNE RB5A/TU-20D) with a resolution of ± 0.05 K, as shown in Fig. 1. Because the copper cylinders ($k \approx 401$ W/m K) are only 0.206 mm thick, the temperature difference between the inner and outer surface of the cylinders is neglected [60–63]. To minimize conduction heat losses through the channel walls, a 25 mm thick polystyrene foam insulation ($k \approx 0.033$ W/m K) is applied to all walls and only the area for flow visualization and a 2 mm thick aperture for the laser sheet is kept without thermal insulation. During the experiment, the steady inflow condition is maintained by means of a constant-head tank that is filled from a reservoir tank using a centrifugal pump. Flow uniformity is achieved with a settling chamber and flow rectifiers placed inside a nozzle with a contraction ratio of 4:1 that is located prior to the channel inlet. The upstream cylinder is located 1.12 m downstream of the channel inlet, which is 10 times the hydraulic diameter, and at a distance of 0.703 m from its center to the outflow boundary. For fluid property evaluation, the temperature of the

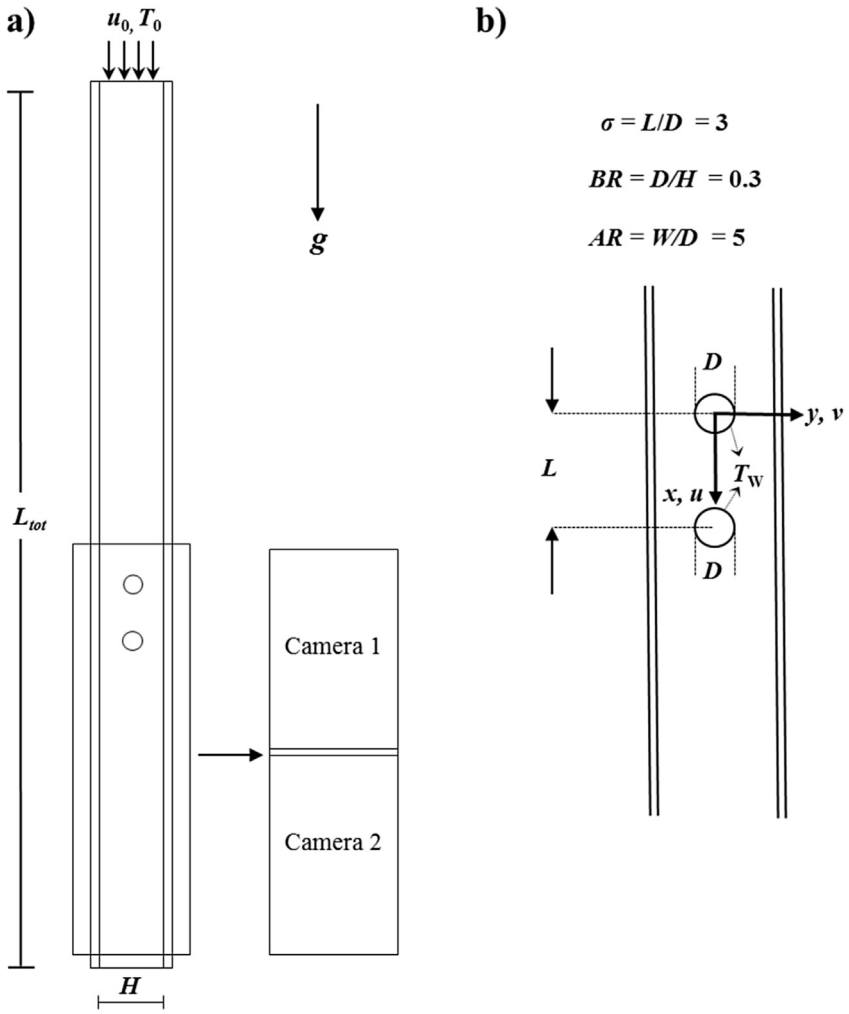

Fig. 2. Size of the images obtained after stitching each image from each camera. The images shown in the next section display a portion of the test section that corresponds to the region demarcated by the black square.

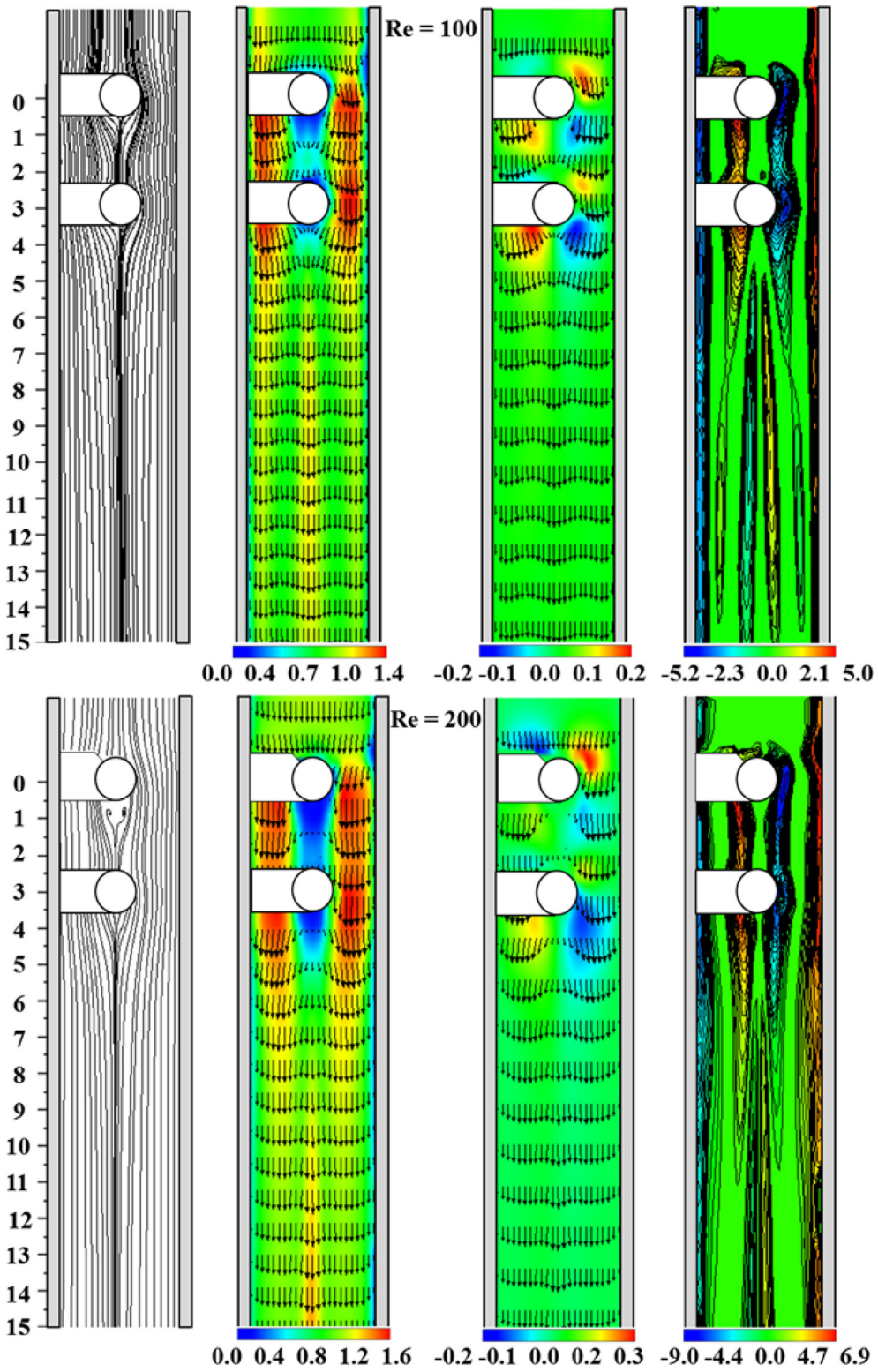

Fig. 3. Nondimensional steady-state flow values at $BR = 0.3$, $\sigma = 3$ and $Ri = -1$ for $Re = 100$ and 200 (top and bottom), respectively. From left to right: streamlines, velocity vector field and vorticity contours, respectively.

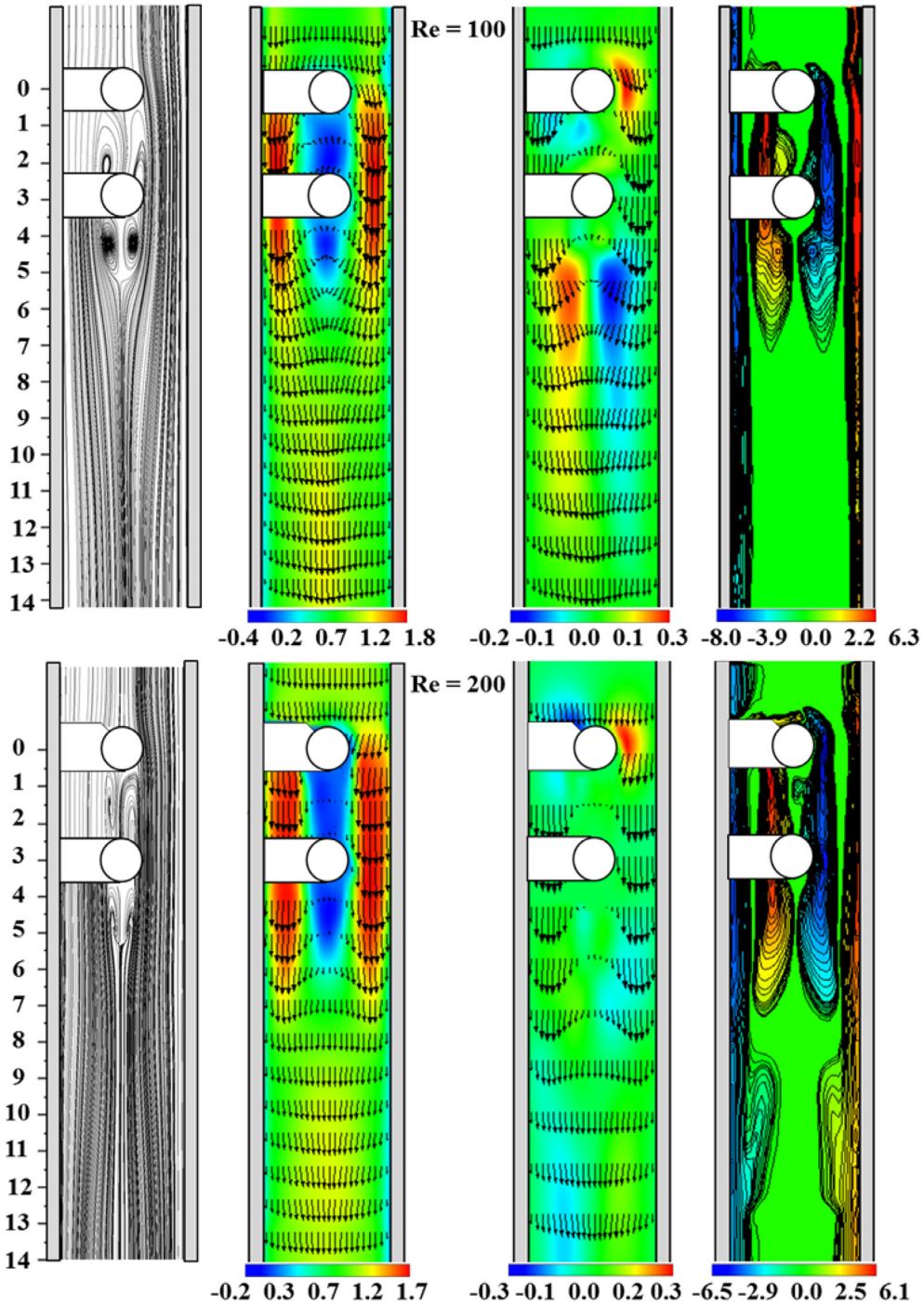

Fig. 4. Nondimensional mean flow values for the unheated cylinders ($Ri = 0$) at $BR = 0.3$ and $\sigma = 3$ for $Re = 100$ and 200 (top and bottom), respectively. From left to right: streamlines, velocity vector field and vorticity contours, respectively.

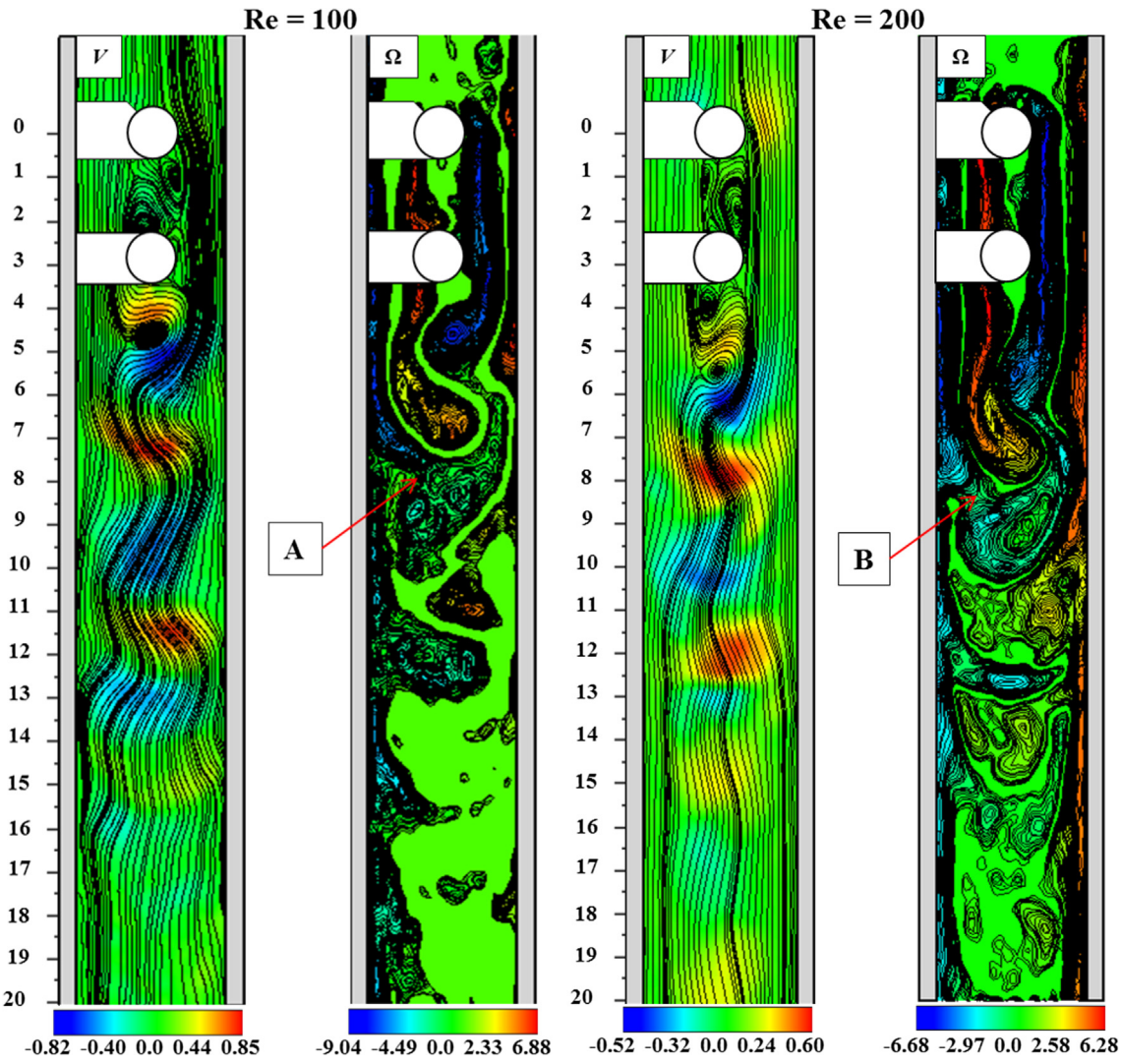

Fig. 5. Nondimensional near wake patterns of instantaneous transverse velocity and vorticity contours for the unheated cylinders ($Ri = 0$) at $BR = 0.3$, $\sigma = 3$, and $Re = 100$ and 200 (left and right), respectively.

water at the inlet of the test section is measured before and after each run using a high-precision thermocouple probe (Control Company, 4132 Traceable® Platinum RTD Thermometer) with a resolution of ± 0.01 K. The measurements are performed after thermal equilibrium is reached between the water that exits the test section and the water in the reservoir tank. This occurs when the heat losses in the circuit equals the heat provided by the cylinders, after approximately 3 h. Because hysteresis effects are anticipated for all combinations of the physical parameters [64–70], for all cases, the measured flow patterns are achieved by proceeding along the same path, starting from a forced convection flow ($Ri = 0$) and adding assisting/opposing buoyancy by monotonically decreasing/increasing the value of the Richardson number. Dumouchel et al. [60] and Wang et al. [71] proposed the use of the effective temperature as a reference temperature for the determination of the fluid properties. However, because its use has not been widely accepted for the determination of vortex shedding from a heated cylinder operating in the mixed convection regime in contra-flow [11,61], all fluid properties are computed based on the thermophysical properties evaluated with the arithmetic mean fluid temperature (average between the temperature at the channel inlet and the temperature of the cylinders). The flow behavior depends on the following independent nondimensional parameters: the Reynolds, Prandtl and Richardson numbers given by $Re = u_0 D/\nu$, $Pr = \nu/\alpha$, and $Ri = g\beta(T_w - T_0)D/{u_0}^2$, respectively (frequently, instead of using the Richardson number, the Grashof number is employed, $Gr = RiRe^2 = g\beta(T_w - T_0)D^3/\nu^2$.) Here, u_0 is the free stream velocity, D is the cylinder diameter, ν the kinematic viscosity, α is the thermal diffusivity, g is the acceleration due to gravity, and β is the thermal expansion coefficient. The Reynolds number is varied by adjusting a valve that regulates the volume flow rate. For a fixed Reynolds number, the Richardson number is modified by varying the temperature difference between the cylinders and the fluid. When $T_w \neq T_0$, buoyancy opposes or assists the

forced flow affecting the flow structure and vortex shedding behind the cylinders. These results are reported and described in the following section.

2.2. Image acquisition

The two-dimensional velocity field measurements are acquired using a Dantec Dynamics PIV system that includes two 14-bit CMOS digital cameras (Phanthom V9.1) with a resolution of 1632 × 1200 pixels and fitted with 60 mm Zeiss lenses that are placed next to each other on mounts with an orientation perpendicular to the measuring plane. The plane is illuminated with a 10 mJ Nd:YLF laser (Litron Lasers) at a wavelength of 527 nm. Using an array of optics, the laser beam is expanded into a diverging light sheet with a thickness of approximately 1 mm. To minimize the scatter of laser light, both cylinders are painted mat-black. Neutrally buoyant polyamide spherical particles of 50 μm in diameter are used as particle tracers. Dantec Dynamics software (DynamicStudio version 3.41) is used to control the cameras and laser for PIV data acquisition and image processing. For all the experiments, single frame image acquisition at a sampling rate of 3 Hz is used. A Dantec Dynamics stitching algorithm is used to overlap the acquired images from each camera with an offset of 2–4 pixels. The stitched images obtained capture the whole channel width, 1.5 cylinder diameters upstream of the first cylinder and 17 cylinder diameters downstream of the second cylinder. The location of the measurement area and the origin of the coordinate system are represented in Fig. 2a and b, respectively. Three datasets of 1000 full-size (14-bit) images are acquired for each value of the Reynolds and Richardson numbers, and the mean velocity distributions in the flow domain are obtained by averaging the total number of images acquired for each set.

2.3. Data processing

The raw displacement vector field is obtained from the recorded PIV data using a Dantec Dynamics adaptive-correlation algorithm with five high accuracy subpixel refinement steps followed by a moving average algorithm that allows for local neighborhood validation using an acceptance factor of 0.12. For each stitched image captured, an interrogation window of 32 × 16 pixels with a 50% horizontal and vertical overlap is used. Spurious velocity vectors (less than 1%) are removed and the vector fields are smoothed using a local a 3 × 3 filter. A total of 7956 (153 × 52) velocity vectors with high spatial resolution are captured over the entire field of view for each stitched image captured. Data validation is carried out using peak validation with a minimum peak height relative to peak 2 of 1.15. Out-of-plane vorticity flow fields are computed from the PIV velocity fields, $\Omega = \partial V/\partial X - \partial U/\partial Y$. Here, Ω is the nondimensional out of plane vorticity and U and V are the nondimensional longitudinal and transverse velocity components associated to the nondimensional X and Y coordinates, respectively. All velocity components are scaled with the inflow velocity, u_0 and X and Y are normalized by D. The computed vectors, velocity and vorticity fields are displayed using Tecplot 360. An estimation of the uncertainties in the experimental parameters is calculated based on the method presented by Kline and McClintock [72]. Our analysis indicates that the experimental uncertainties at a 95% confidence level for the Reynolds, Grashof and Richardson numbers are 1.4%, 3.7% and 3.3%, respectively.

3. Results

The experimental results presented in this work correspond in all cases to $Pr = 7$, $BR = 0.3$, $AR = 5$, and $\sigma = 3$. In this section, results for the mean and instantaneous flow characteristics are presented for $Re = 100$ and 200 under varying thermal buoyancy.

3.1. Response characteristics for assisting flow ($Ri = -1$)

In the following subsection, the response characteristics for assisting flow with $Ri = -1$ are presented. Fig. 3 shows for $Re = 100$ and 200 the resulting nondimensional steady-state flow values at $Ri = -1$ in the nondimensional X–Y plane located at the middle of the cylinders' span. For clarity, only a portion of the final stitched image is shown. The velocity and vorticity fields are displayed together, and the color scales below each image map the velocity and vorticity contours. The images display (from left to right) the streamlines, the nondimensional longitudinal and transverse velocity fields with superimposed vectors, and the nondimensional vorticity contours. For both values of Re, because the vortex street is always suppressed, a steady state symmetric solution exists, and the near wake of the upstream cylinder is smaller than the near wake of the downstream one. Note how because of the narrow downflow of cold fluid, the longitudinal velocity component

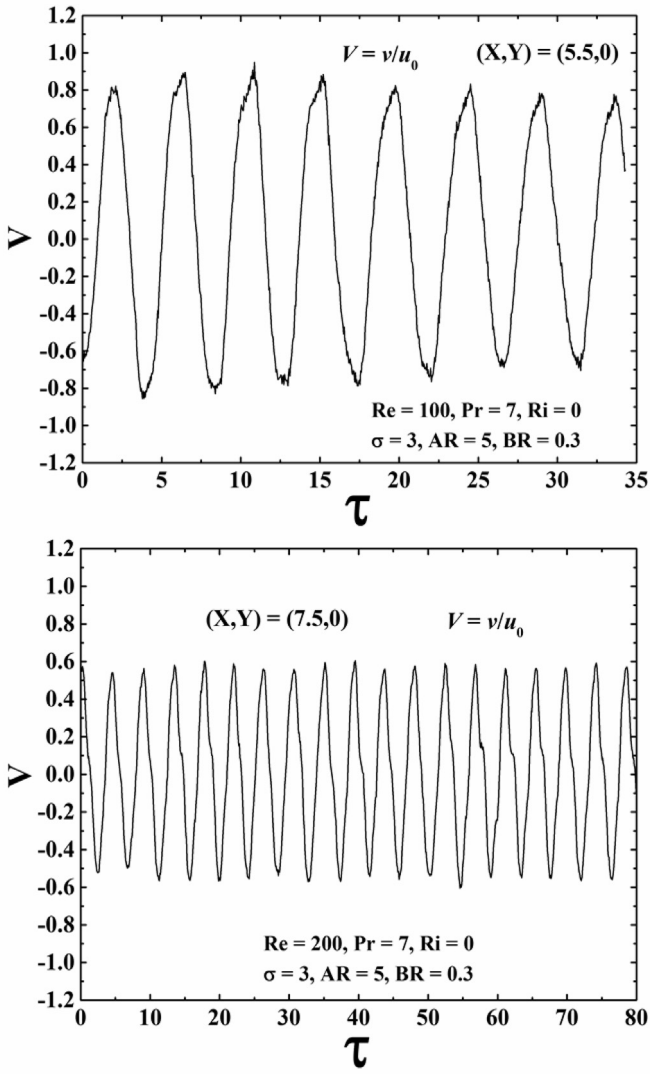

Fig. 6. $BR = 0.3$, $\sigma = 3$ and $Ri = 0$ for $Re = 100$ and 200 (top and bottom), respectively. Time variations of the nondimensional transverse velocity component as a function of the nondimensional time. The extracted data is obtained at the symmetry plane and different X positions.

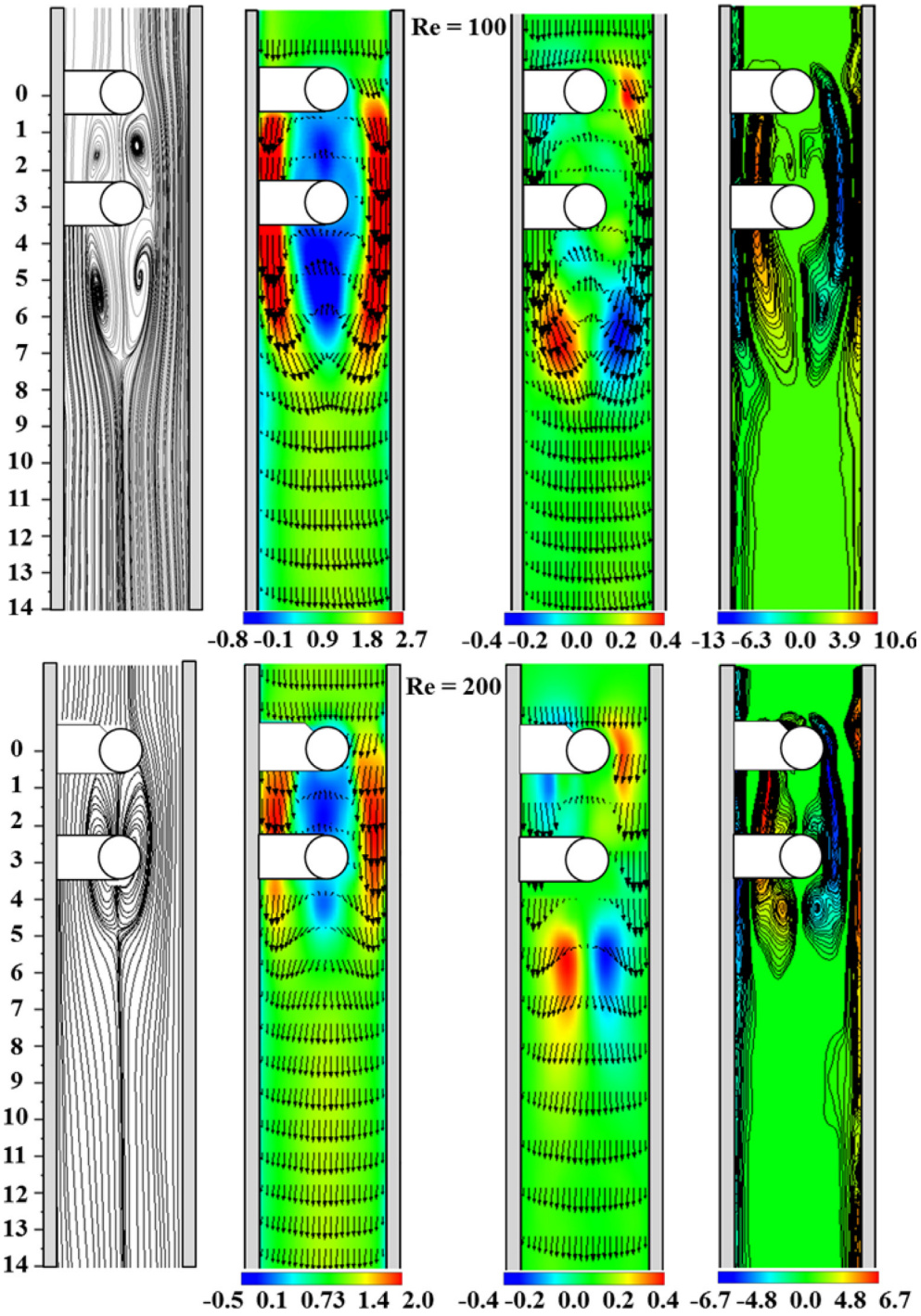

Fig. 7. Nondimensional mean flow values at $BR = 0.3$, $\sigma = 3$ and $Ri = 1$ for $Re = 100$ and 200 (top and bottom), respectively. From left to right: streamlines, velocity vector field and vorticity contours, respectively.

increases at the central part of the channel ($Y = 0$) towards the downstream direction. For $Re = 100$, flow separation is delayed and no flow reversal is found in the flow patterns. For $Re = 200$, although the flow does not separate behind the downstream cylinder, the presence of a small recirculation zone at the rear of the upstream cylinder is evident.

3.2. Response characteristics for a pure forced convection flow ($Ri = 0$)

Fig. 4 shows the nondimensional mean flow values at $Ri = 0$ (isothermal flow). In the absence of buoyancy and for both values of Re, symmetric recirculation zones are present behind both cylinders, the recirculation zone of the upstream cylinder occupies the total space within the gap, and the near wake of the downstream cylinder is tangibly shorter and narrower than that produced by the upstream one. The streamline patterns show a wider recirculation zone for $Re = 100$, which explains why the relative maximum downward flow velocity and peak vorticity values are higher for the lower value of Re. In this figure, the fourth strips show the shear layers generated by the upstream cylinder impinging the forebody of the downstream cylinder. Also, because of the channel blockage, a relatively small interaction between the vorticity generated at the forebody of the upstream cylinder and the confining channel walls takes place. Fig. 5 shows for $Re = 100$ and 200 the vortex shedding process for the cylinder array in the absence of any heat input ($Ri = 0$) by displaying typical nondimensional instantaneous patterns of transverse velocity contours with superimposed streamlines and vorticity contours for the same time. For both values of Re, vortices are shed from the upstream cylinder and a Kármán vortex shedding pattern takes place at the rear of the downstream cylinder. In these figures, **A** and **B** highlight how at $X \approx 9$, vorticity generated at the channel walls merges with the downstream vortices with the same sign. Fig. 6 shows for $Ri = 0$ the time variations of the nondimensional transverse velocity component at the symmetry plane as a function of the nondimensional time tu_0/D. For $Re = 100$ and 200, the extracted data is obtained at a location of $(X,Y) = (5.5,0)$ and $(X,Y) = (7.5,0)$, respectively. Clearly, the velocity fluctuations are almost monochromatic, with the relative amplitude of the oscillations being higher for $Re = 100$. A spectral analysis of the oscillations is obtained from the measured instantaneous transverse velocity sampled at the locations mentioned above. The Strouhal number, $St = fD/u_0$ relates the characteristic oscillation frequency f to the inverse of the flow

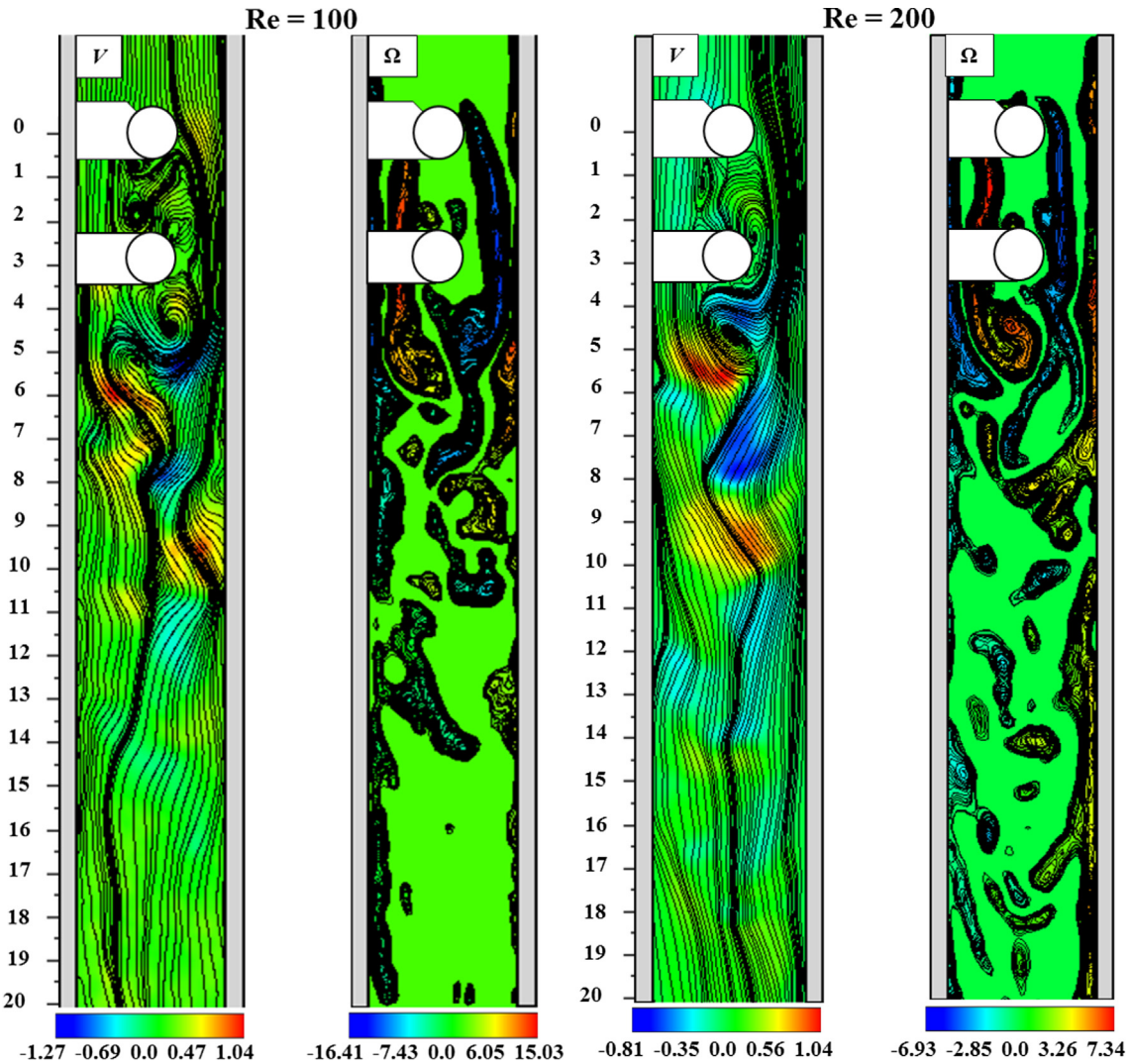

Fig. 8. Nondimensional near wake patterns of instantaneous transverse velocity and vorticity contours at $Ri = 1$ showing the shed vortex structures for $Re = 100$ and 200 (left and right), respectively.

residence time, u_0/D, and it is obtained from the normalized amplitude of the fast Fourier transform (FFT) of the transverse velocity signal. The FFT is obtained from 1000 samples. For $Re = 100$ and 200, there is a peak at $St = 0.224$ and $St = 0.230$ (time period close to 4.47 and 4.34 times the residence time), respectively. The presence of these peaks indicates that for the unheated cylinders, the vortex shedding of the downstream cylinder is time periodic and is mainly dominated by a single fundamental frequency.

3.3. Response characteristics for opposing flow ($1 \leq Ri \leq 3$)

In this subsection, the response characteristics for opposing thermal buoyancy are presented for increasing values of the Richardson number. Fig. 7 shows the nondimensional mean flow values for $Ri = 1$ and $Re = 100$ and 200, respectively. For $Re = 100$, the flow at the surface of the upstream cylinder separates earlier, the recirculation zone that occupies the total space within the gap becomes considerably wider than that for the isothermal case, and the recirculation zone of the downstream cylinder is now larger than the recirculation zone present at the gap. Hence, the blockage effect increases and a maximum downward flow velocity that is reached next to the channel gaps increases to $U = 2.67$, while a minimum upward flow velocity of $U = -0.80$ is observed at $X \approx 4.75$. Also, vorticity strength increases and the interaction between the shear layers generated by the upstream cylinder and the confining walls steps up and overshoots the downstream cylinder without reattaching to the latter. For $Re = 200$, the recirculation zones of both cylinders increase their width and strength too. These images exemplify how because of the fact that the Richardson number remains fixed, as the value of the Reynolds number increases from $Re = 100$ to 200, the Grashof number increases accordingly. As a result, enhanced flow reversal takes place and the recirculation zone present at the rear of the downstream cylinder becomes shorter. Also, the interaction between vorticity generated by the upstream cylinder and the confining walls is slightly lower for this higher Re. Fig. 8 shows for $Re = 100$ and 200 the instantaneous near wake patterns at $Ri = 1$ by displaying typical nondimensional transverse velocity contours with superimposed streamlines and vorticity contours for the same time. For both values of Re, the affected flow field by the buoyancy force results in a shorter wake behind the downstream cylinder and the periodic alternate shedding of vortices still depicts a Kármán vortex street. Fig. 9 shows for both values of Re and $Ri = 1$ the time variations of the nondimensional transverse velocity component as a function of the nondimensional time. In this figure, the extracted data for $Re = 100$ and 200 is obtained at sampling locations of $(X,Y) = (6.5,0)$ and $(X,Y) = (7.5,0)$, respectively. Although an established periodicity is evident, the time traces of the velocity signals depict glitches that appear due to the superimposed opposing buoyancy force. The wake velocity spectra of the transverse velocity signal for $Re = 100$ and 200 features two peaks at $St = 0.267$ and $St = 0.218$ (time period close to 3.75 and 4.59 times the residence time), respectively. These peaks indicate that for this value of Ri, the vortex shedding is time periodic and is still dominated by a single fundamental frequency. Fig. 10 shows the nondimensional mean flow values for $Ri = 2$ and $Re = 100$ and 200, respectively. For $Re = 100$, enhanced flow reversal occurs, the flow separates earlier at the surface of the upstream cylinder, the width of the recirculation zones present at the gap and behind the downstream cylinder increase too, and the maximum and minimum values of the mean vorticity field also increase. For $Re = 200$, an increase in the width of the recirculation zones behind each cylinder takes place, the downstream cylinder is completely surrounded with upward flow velocity, the length of the recirculation zone of the latter increases, and the peak vorticity values step up. Interestingly, due the

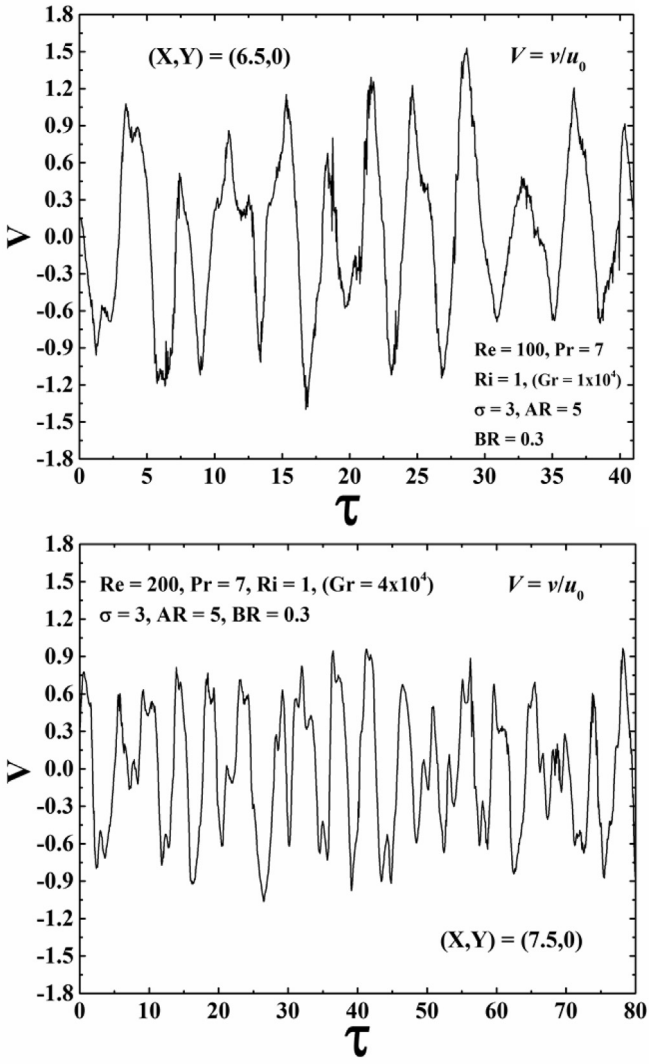

Fig. 9. $BR = 0.3$, $\sigma = 3$ and $Ri = 1$ for $Re = 100$ and 200 (top and bottom), respectively. Time variations of the nondimensional transverse velocity component as a function of the nondimensional time. The extracted data is obtained at the symmetry plane and different X positions.

fact that the mean wakes are wider for $Re = 100$ than for $Re = 200$, higher peak values of the velocity and vorticity fields are registered for the lower Re. Fig. 11 shows the instantaneous near wake patterns at different time instants for $Ri = 2$ and $Re = 100$ and 200, respectively. For $Re = 100$, significant differences in the dynamics of the wake take place. Upper Fig. 11a) shows the shed vortices traveling downstream. Here, due to the strong opposing buoyancy, their velocity reduces, they are captured by the new formed vortices, and a larger vortical structure that flows downstream with reduced speed is produced. This process is shown in upper Fig. 11b), where the instantaneous streamlines display a wake pattern with three relatively large recirculation bubbles interacting at the same time prior to merging into a larger vortical structure. In addition, the strong interaction between the shear layers generated by the upstream cylinder and the confining walls increase the peak vorticity values. For $Re = 200$, the streamline pattern in lower Fig. 11a) shows that the wake pattern of the downstream cylinder has two vortices that are being shed in an alternating way. However, lower Fig. 11b) shows that instead of an alternate shedding of vortices, because of the instability originating at the wake, the

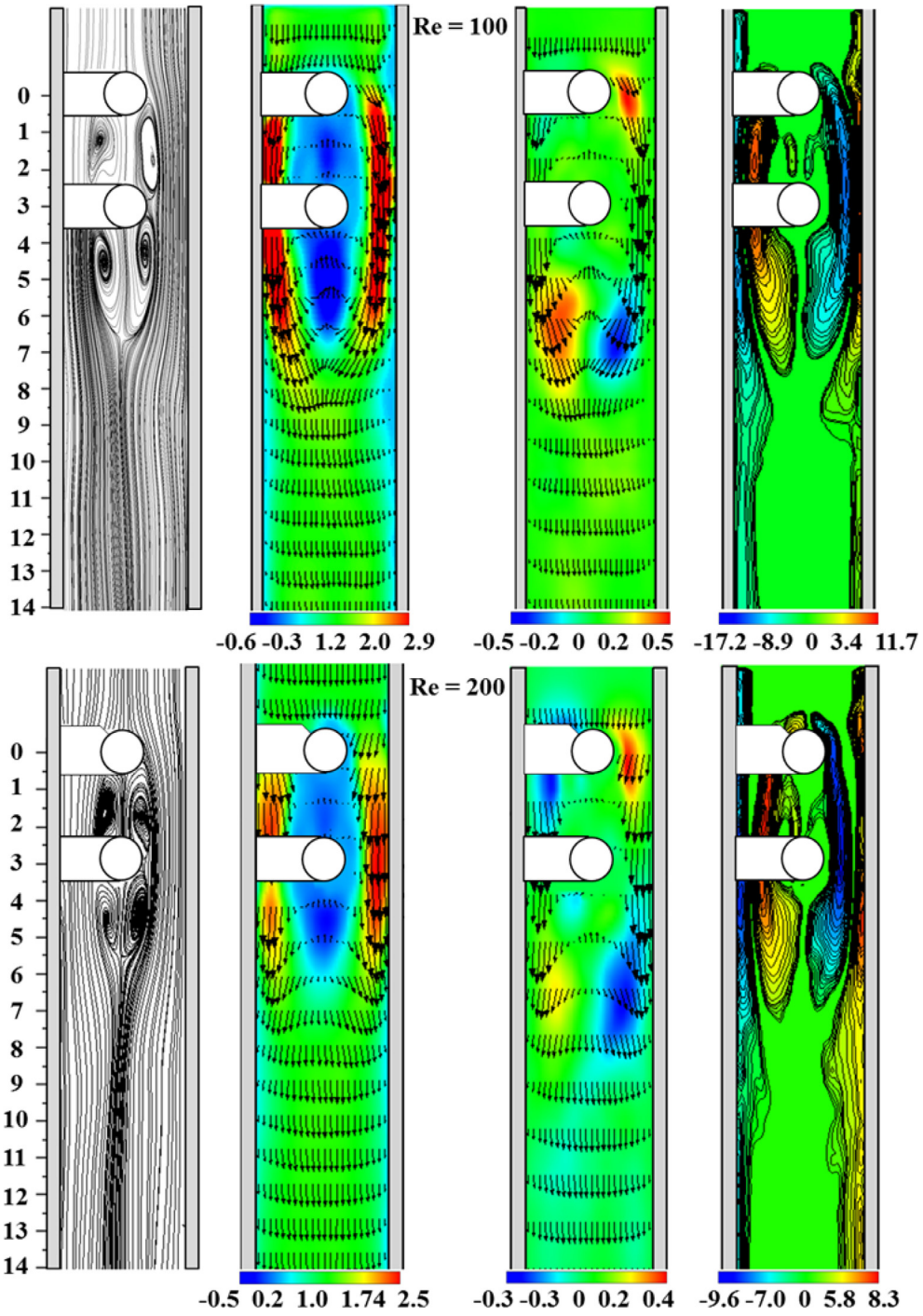

Fig. 10. Nondimensional mean flow values at $BR = 0.3$, $\sigma = 3$ and $Ri = 2$ for $Re = 100$ and 200 (top and bottom), respectively. From left to right: streamlines, velocity vector field and vorticity contours, respectively.

streamline pattern depicts two vortices at the rear of the downstream cylinder that are being shed at the same time. Fig. 12 shows for $Ri = 2$ the time variations of the nondimensional transverse velocity component as a function of the nondimensional time. In this figure, the extracted data for $Re = 100$ and 200 is obtained at sampling locations of $(X,Y) = (8.5,0)$ and $(X,Y) = (9.5,0)$, respectively. For $Re = 100$, the typical time history shows that the vortex shedding pattern is characterized by the presence of glitches in the periodic signal. A peak at $St = 0.121$ (time period close to 8.25 times the residence time) of the corresponding wake velocity spectra of the transverse velocity signal indicates that the vortex shedding still has an established periodicity of relatively low frequency. The bottom image shows that the presence of glitches in the time traces of the periodic velocity signal is evident for $Re = 200$. The wake velocity spectra of the transverse velocity signal features two peaks at $St = 0.267$ and $St = 0.291$ (time period close to 3.75 and 3.44 times the residence time), respectively. These peaks indicate that for this value of Ri, because of the reversed flow that moves upstream, the vortex shedding presents quasi-periodic motion of relatively high frequency. Fig. 13 shows the nondimensional mean

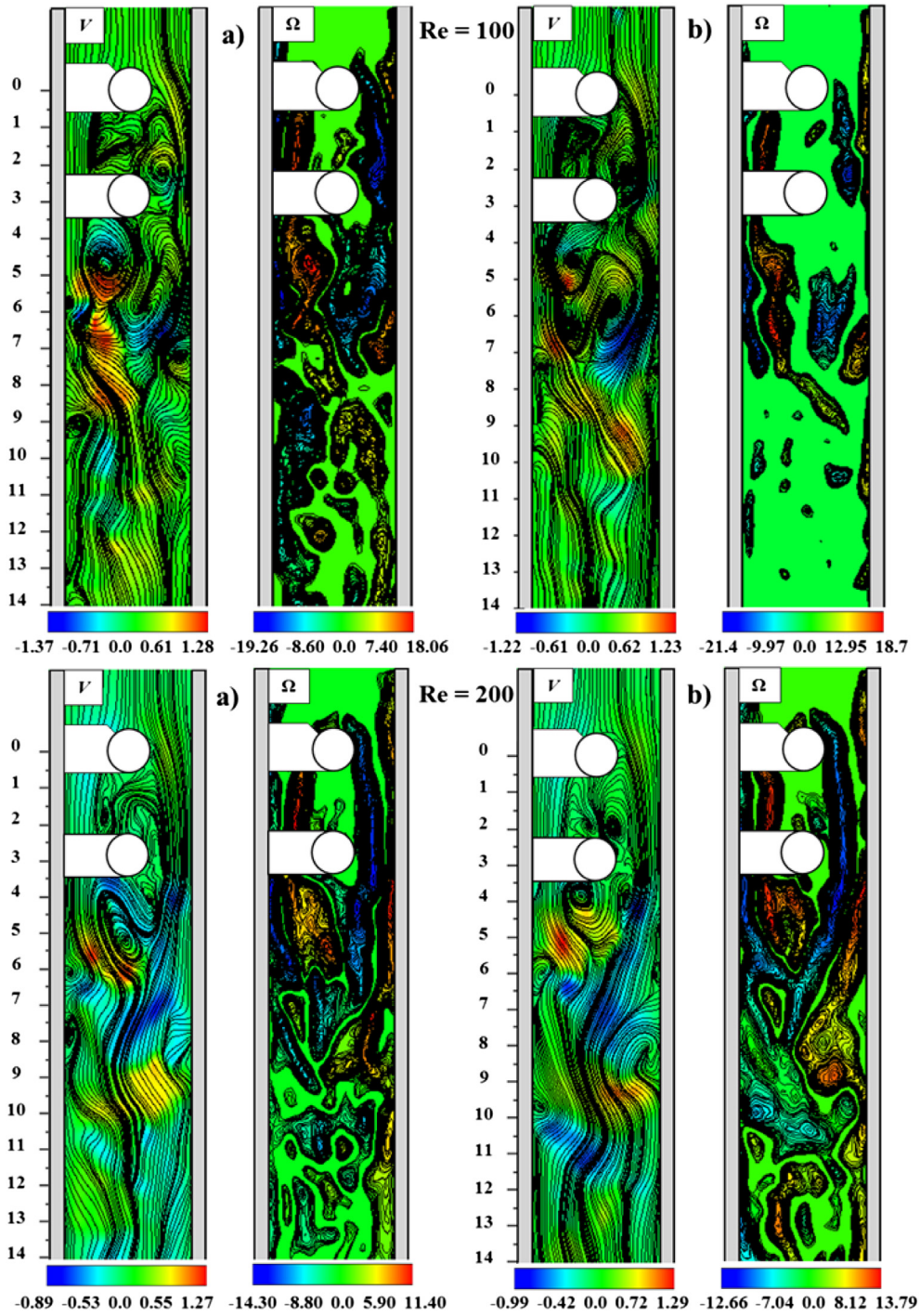

Fig. 11. Nondimensional near wake patterns of instantaneous transverse velocity and vorticity contours at $Ri = 2$ showing the shed vortex structures at different time instants for $Re = 100$ and 200 (top and bottom), respectively.

flow values for $Ri = 3$ and both values of Re. For this higher value of buoyancy strength, the flow at the surface of the upstream cylinder separates earlier. This happens because of the upward buoyant flow within the gap region between the two cylinders that penetrates upstream. For $Re = 100$, as the value of Ri increases, the width and length of the recirculation zone behind the downstream cylinder decreases. However, the opposite trend is observed for $Re = 200$, i.e., the size of the near wake of the downstream cylinder increases with increasing buoyancy. Fig. 14 shows the time variations of the nondimensional longitudinal and transverse velocity components as a function of the nondimensional time for $Ri = 3$ and both values of Re. For $Re = 100$ and 200, the extracted data is obtained at sampling locations of $(X,Y) = (8.5,0)$ and $(X,Y) = (9.5,0)$, respectively. In this figure, the time traces of the velocity signals clearly indicate that due to the strong opposing buoyancy, the vortex shedding pattern behind the downstream cylinder has become irregular.

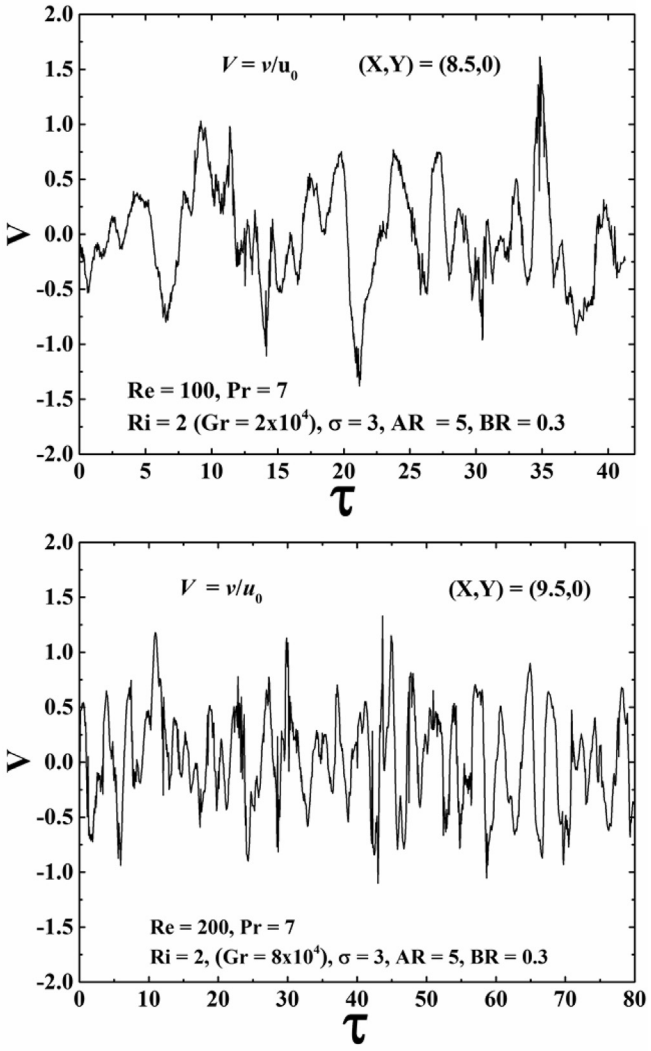

Fig. 12. $BR = 0.3$, $\sigma = 3$ and $Ri = 2$ for $Re = 100$ and 200 (top and bottom), respectively. Time variations of the nondimensional transverse velocity component as a function of the nondimensional time. The extracted data is obtained at the symmetry plane and different X positions.

3.4. Time-averaged wake centreline velocities

Fig. 15 shows for both values of *Re* and several values of the Richardson number the nondimensional time-averaged streamwise velocities along the vertical axis in front of the upstream cylinder, within the gap and in the wake region of the symmetry plane towards the downstream direction. Clearly, for $Ri = 0$ and up to $Ri = 4$, the space within the gap is totally occupied by the recirculation zone of the upstream cylinder for both values of *Re*. For $Re = 100$ and assisting buoyancy, only positive values of the longitudinal velocity component are detected along the symmetry plane, and the longitudinal velocity within the gap reaches a peak value of $U = 0.43$ at $X \approx 1.92$. For $Ri = 0$ and $Ri = 0.5$, the recirculation zone of the downstream cylinder extends to $X \approx 5.07$ and $X \approx 5.34$, respectively. Note how for this parameter values, the strength of the recirculation zone of the downstream cylinder is slightly lower than that for the upstream one. By further increasing the value of the buoyancy parameter to $Ri = 1$ and 1.5, the mean near wake of the downstream cylinder increases accordingly. However, as the Richardson number is further increased to $Ri = 2$ and $Ri = 3$, the size of the near wake of the downstream cylinder decreases for increasing values of buoyancy strength. For $Re = 200$ and $Ri = -1$, a short recirculation zone appears behind the upstream cylinder. However, only positive values of the longitudinal velocity component are detected at the rear of the downstream cylinder. For the unheated cylinders ($Ri = 0$), the recirculation zone of the downstream cylinder extends to $X \approx 5.29$, and the latter is now stronger than the one present within the gap. As the buoyancy parameter increases to $Ri = 0.5$ and $Ri = 1$, the extent of the recirculation zone of the downstream cylinder decreases to $X \approx 5.14$ and $X \approx 4.85$, respectively. By further increasing the value of the Richardson number to $Ri = 2$ and $Ri = 3$, the mean near wake of the downstream cylinder extends to $X \approx 5.58$ and $X \approx 6.17$, respectively. Note that for all cases, the time-averaged wake centreline velocities increase downstream and fully recuperate at $X \approx 10$. Also, for all values of *Ri*, no flow reversal has been observed at the top of the upstream cylinder, which indicates that opposing buoyancy cannot develop a recirculation bubble due to the strong shear produced by the cold down flow.

3.5. Wake closure lengths

Fig. 16 shows for $Re = 100$ and 200 the mean nondimensional wake closure length of the downstream cylinder $\sigma_{v2} = L_{v2}/D$, as a function of the Richardson number. Here, L_{v2} is defined as the streamwise distance from the axis of the downstream cylinder to the point where the mean centerline velocity changes from negative values to zero. The measurement of the wake closure length is obtained based on the statistical average from 3 datasets of 1000 images for each value of *Ri*, and results are presented as mean $\pm$ *SD*. For assisting buoyancy and for both values of *Re*, no flow reversal is detected behind the downstream cylinder. For $Re = 100$ and $Ri = 0$, the wake closure length is ~ 1.70 cylinder diameters. For $Ri = 0.5$, the wake closure length slightly increases to ~ 2.34. However, for $Ri = 1$ and $Ri = 1.5$, the near wake of the downstream cylinder is tangibly larger and the wake closure length increases to ~ 3.49 and ~ 4.40, respectively. By further increasing the buoyancy parameter to $Ri = 2$ and $Ri = 3$, due to the strong opposing buoyancy, the wake closure length reduces to ~ 3.68 and ~ 2.54, respectively. For $Re = 200$ and $Ri = 0$, the wake closure length is ~ 2.28 cylinder diameters. Note how for this higher value of *Re*, as the buoyancy parameter increases to $Ri = 0.5$ and $Ri = 1$, its size reduces to ~ 2.14 and 1.85, respectively. However, for increasing values of the Richardson number of $Ri = 1.5$, 2 and 3, the near wake increases accordingly and the wake closure length extends to ~ 1.99, 2.58 and 3.17 cylinder diameters, respectively. A summary of Fig. 16 is shown in Table 1. Here, $\sigma_{v1} = L_{v1}/D$ corresponds to the nondimensional wake closure length of the upstream cylinder. Also, the maximum value of flow reversal within the gap and at the rear of the downstream cylinder are denoted by U_{min1} and U_{min2}, respectively, and X_{min1} and X_{min2} make reference to the streamwise location along the vertical axis where the highest upward flow takes place behind each cylinder.

3.6. Separation angle

The position of the separation angle θ_s, is measured from the front stagnation point of each cylinder to the separation point (position where reversed flow gradient is detected at the surface of the cylinders). As the separation angle varies with time because of vortex shedding, the mean value of the separation angle is obtained using the time-averaged streamline patterns and contour plots of the streamwise velocity component. A total of 3 datasets of 1000 images are used to obtain the arithmetic mean of the separation angle for each value of the buoyancy parameter. Table 2 shows for both values of *Re* the relationship between the averaged separation

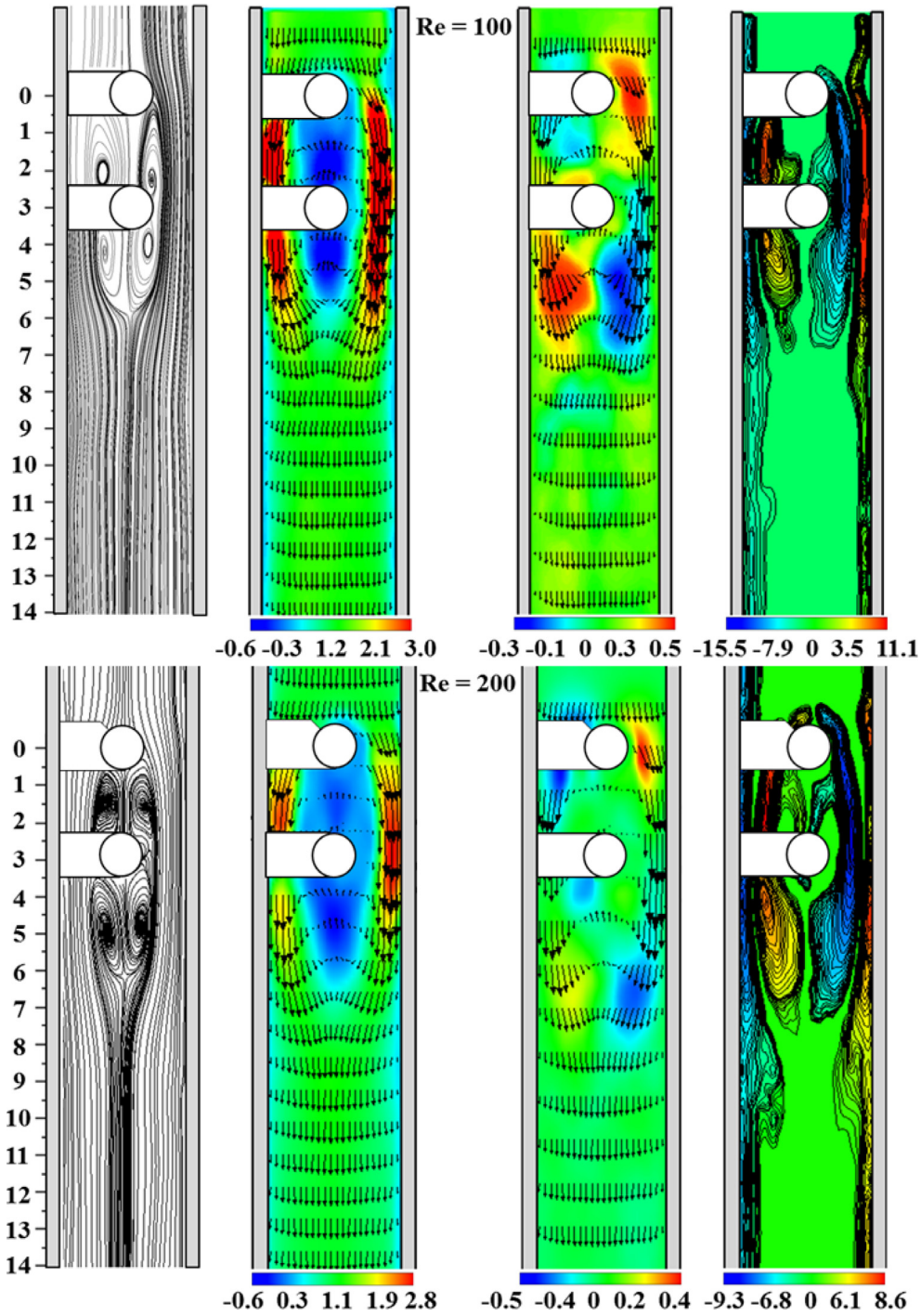

Fig. 13. Nondimensional mean flow values at $BR = 0.3$, $\sigma = 3$ and $Ri = 3$ for $Re = 100$ and 200 (top and bottom), respectively. From left to right: streamlines, velocity vector field and vorticity contours, respectively.

angle $\pm$ *SD* as a function of the Richardson number. For the case of assisting buoyancy, because of the fact that the temperature of both cylinders exerts a favorable pressure gradient, the value of the separation angle for both cylinders reaches a maximum, with the highest value reached at the downstream cylinder. However, the separation angle decreases monotonically for increasing values of the Richardson number in the range $0 \leq Ri \leq 3$. It is worth mentioning that for both values of *Re* and Richardson numbers of $Ri = 1$ and higher, because the shear layers that separate from the upstream cylinder overshoot the downstream cylinder, no separation angle is reported for the latter.

3.7. Strouhal number or shedding frequency

The mean value of the measured Strouhal number $\pm$ *SD* as a function of the Richardson number for both values of *Re* is shown in Table 3. For $Re = 100$ and $Ri = -1$, a steady-state flow response is reached. For $Ri = 0$, a periodic oscillatory flow response is reached, and the corresponding Strouhal number is of $St = 0.222$. As the value of the buoyancy parameter increases to $Ri = 1$, the flow

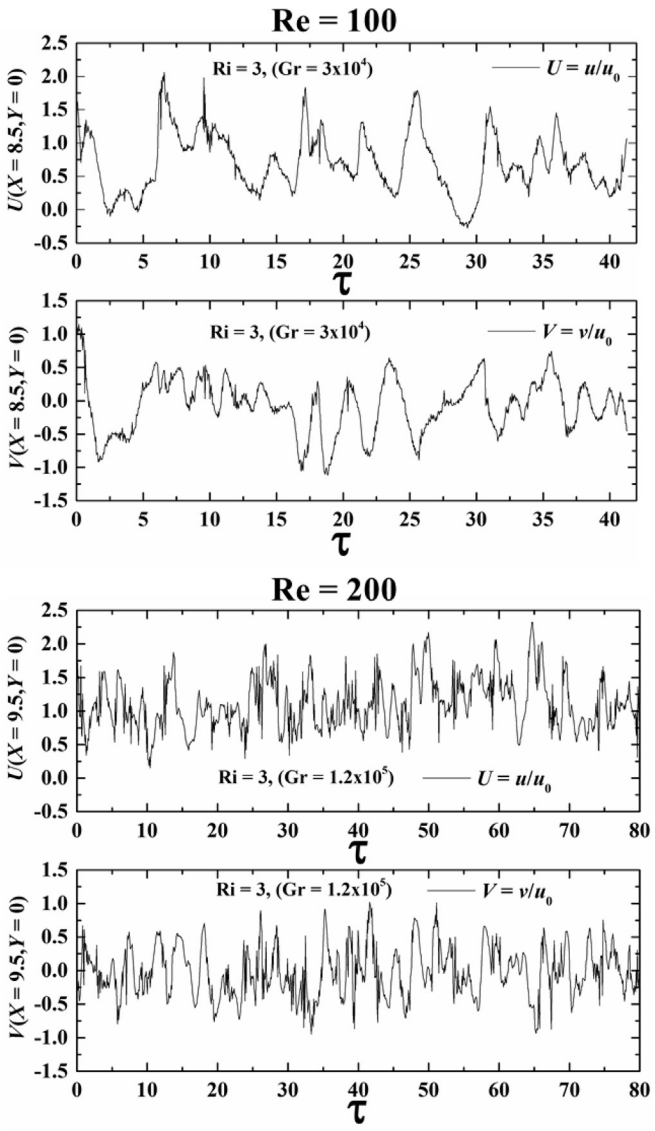

Fig. 14. Time variations of the nondimensional longitudinal and transverse velocity components as a function of the nondimensional time for $Ri = 3$ at $Re = 100$ and 200 (top and bottom), respectively. The extracted data is obtained at the symmetry plane and different X positions.

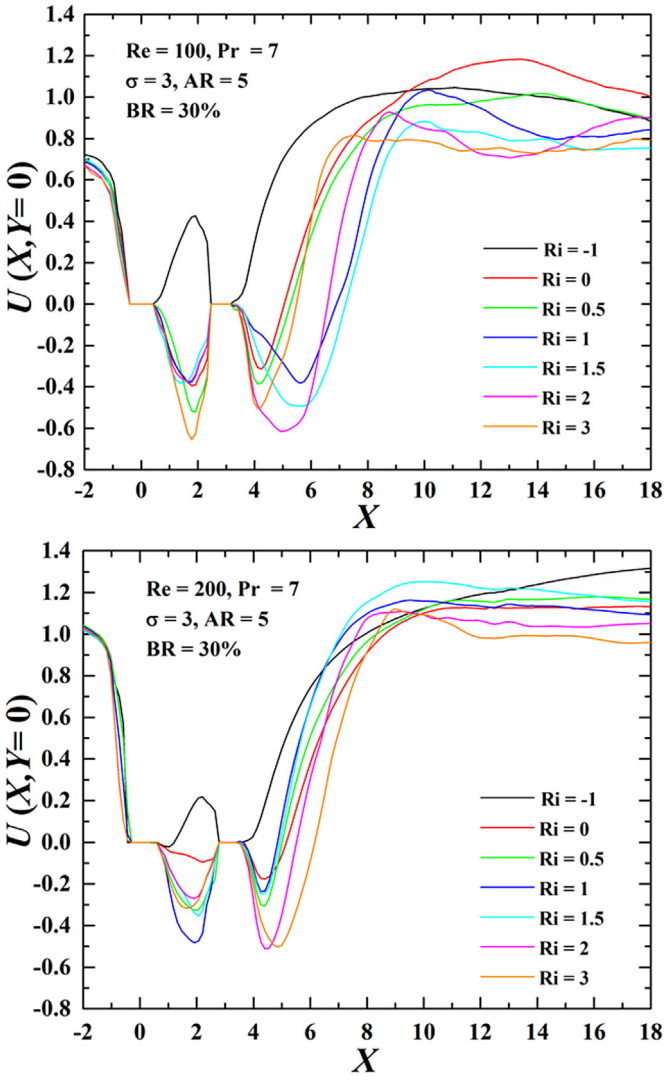

Fig. 15. Mean nondimensional streamwise velocity profiles along the wake centerline as a function of the nondimensional longitudinal coordinate for different Richardson numbers at $Re = 100$ and 200 (top and bottom), respectively.

response is still time-periodic and the Strouhal number increases accordingly. However, by further increasing the buoyancy strength to $Ri = 2$, the Strouhal number drops dramatically. For the highest value of the Richardson number of $Ri = 3$, the wake shedding pattern is characterized by the lack of periodicity. For $Re = 200$ and $Ri = -1$, a steady-state flow response is reached, while for values of $Ri = 0$ and up to $Ri = 2$, the Strouhal number increases for increasing values of the buoyancy parameter. Finally, an irregular wake pattern sets in for $Ri = 3$.

3.8. Comparison of experimental data with numerical results

In this subsection, comparison between the experimental data and numerical results for the same parameter values is presented. Details of the numerical solution can be found elsewhere [58,59]. The two-dimensional computations indicate that for values of the buoyancy parameter higher than $Ri = 1$, important differences in the flow motion appear, which indicate that the role of the three-dimensionality of the flow due to wall effects becomes very pronounced. Table 4 displays the measured Strouhal numbers and the corresponding two-dimensional simulation results for both values of Re and Richardson numbers in the range $-1 \leq Ri \leq 1$. Given all the parameters contributing to uncertainty in estimation of the Strouhal number and that numerical predictions specify a Poiseuille parabolic velocity profile at the channel inlet, the error between experimental data and numerical simulations are deemed an excellent outcome in the current study.

3.9. Aspect ratio effect

In this subsection, the effect of small aspect ratio on the vortex shedding along the span of the cylinders is presented for both values of Re and several values of the buoyancy parameter. Figs. 17–19 show the time-averaged flow patterns measured in the X-Z plane that goes through the cylinders' axes. In these figures and for each value of Re, the left and right images display the longitudinal velocity field with superimposed streamlines and the spanwise velocity fields with superimposed velocity vectors, respectively. Here, the blue/red color represents negative/positive

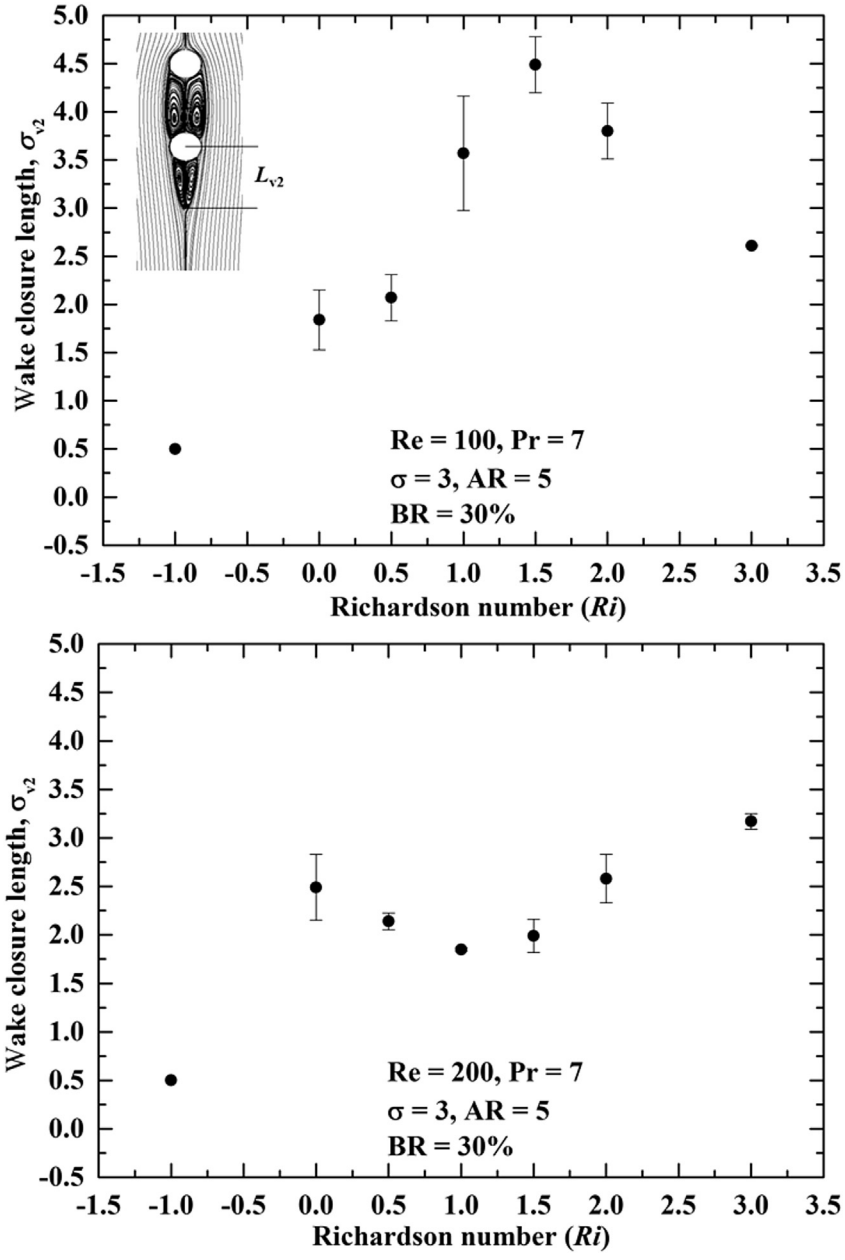

Fig. 16. Nondimensional wake closure length of the downstream cylinder σ_{v2}/D as a function of the Richardson number displayed as mean ± *SD* for $Re = 100$ and 200 (top and bottom), respectively. The length is measured form the center of the downstream cylinder.

Table 1
Summary of the measured mean flow values for $Re = 100$ and 200 as a function of the Richardson number. Here, σ_{v1} and σ_{v2} correspond to the nondimensional wake closure length of the upstream and downstream cylinder, respectively, U_{min1} and U_{min2} denote the maximum value of flow reversal within the gap and at the rear of the downstream cylinder, respectively, and X_{min1} and X_{min2} make reference to the streamwise location along the vertical axis where the highest upward flow takes place behind each cylinder.

Re	*Ri*	σ_{v1}	U_{min1}	X_{min1}	σ_{v2}	U_{min2}	X_{min2}
100	−1	–	–	–	–	–	–
100	0	–	−0.39	1.92	1.70	−0.31	4.25
100	0.5	–	−0.52	1.92	1.99	−0.39	4.11
100	1	–	−0.38	1.78	3.49	−0.38	5.61
100	1.5	–	−0.38	1.37	4.40	−0.49	5.61
100	2	–	−0.38	1.64	3.68	−0.62	4.93
100	3	–	−0.65	1.78	2.54	−0.51	4.11
200	−1	1.32	−0.02	1.03	–	–	–
200	0	–	−0.09	2.20	2.28	−0.18	4.40
200	0.5	–	−0.33	1.91	2.14	−0.31	4.41
200	1	–	−0.48	1.91	1.85	−0.24	4.26
200	1.5	–	−0.36	2.08	1.99	−0.25	4.26
200	2	–	−0.27	1.91	2.58	−0.51	4.41
200	3	–	−0.32	1.76	3.17	−0.50	4.85

Table 2
Separation angle (in degrees) of the upstream and downstream cylinders as a function of the Richardson number for $Re = 100$ and 200.

		Separation angle (mean ± *SD*)	
Re	*Ri*	Upstream cylinder	Downstream cylinder
100	−1	142.00 ± 0.82	157.66 ± 2.05
100	0	138.66 ± 0.47	146.00 ± 0.82
100	0.5	131.33 ± 0.47	152.33 ± 0.47
100	1	105.66 ± 0.47	–
100	1.5	89.33 ± 0.50	–
100	2	84.50 ± 0.56	–
100	3	82.66 ± 0.6	–
200	−1	154.66 ± 0.47	157.33 ± 1.01
200	0	135 ± 0.82	137.66 ± 1.09
200	0.5	125.66 ± 1.70	134.33 ± 1.25
200	1	118.66 ± 0.47	–
200	1.5	117.66 ± 0.50	–
200	2	116.01 ± 0.05	–
200	3	97.66 ± 2.05	–

Table 3
Strouhal number for $Re = 100$ and 200 as a function of the Richardson number.

Re	*Ri*	*St* (mean ± *SD*)
100	−1	steady-state
100	0	0.222 ± 0.007
100	1	0.258 ± 0.014
100	2	0.122 ± 0.002
100	3	irregular wake pattern
200	−1	steady-state
200	0	0.234 ± 0.007
200	1	0.226 ± 0.007
200	2	0.283 ± 0.014
200	3	irregular wake pattern

Table 4
Comparison between experimental data and numerical results for $Re = 100$ and 200 as a function of the Richardson number.

		Experimental data	Numerical results 58, 59	% Error
Re	*Ri*	*St*	*St*	
100	−1	steady-state	steady-state	0
100	0	0.222 ± 0.007	steady-state	–
100	1	0.258 ± 0.014	0.243	6.04
200	−1	steady-state	steady-state	0
200	0	0.234 ± 0.007	0.247	5.37
200	1	0.226 ± 0.007	0.243	7.39

velocity values. Fig. 17 shows the time-averaged flow pattern at $Ri = -1$ (top images) and $Ri = 0$ (bottom images). For $Re = 100$, small regions with almost zero velocity are present behind both cylinders and a sharp increase in the value of the longitudinal velocity component close to the confining walls takes place towards the downstream direction. For $Re = 200$, the region with almost zero velocity occupies the total space within the gap. Note how for this higher *Re*, the almost zero velocity region located at the rear of the downstream cylinder is slightly slanted with respect to the axis of the latter, being longer close to the end walls and shorter at the midspan region. In Fig. 17, the mean flow patterns for $Ri = 0$ show how in the absence of buoyancy, parallel vortex shedding over the entire span of the cylinders takes place. For $Re = 200$, due to changes in the thickness of the boundary layer on the sidewalls, two cells are observed along the span of both cylinders, with their junction occurring at the midspan region. Fig. 18 shows for $Ri = 1$ (top images) and $Ri = 2$ (bottom images) the spatial development of the boundary layer on both walls. For $Re = 100$, the parallel-shedding mode is destroyed by the opposing buoyancy, the shed cells are larger at the midspan region than those located close to the end walls, and the oblique-shedding mode sets in. For $Re = 200$, although the vortex shedding is still not in phase along the span, enhanced flow reversal takes place close to the end walls and recirculation zones develop in the *X-Z* plane within the gap. For $Ri = 2$, a drastic change in the wake structure takes place depending on the value of *Re*. For $Re = 100$, the shedding pattern within the gap is highly irregular, which indicates that the shedding pattern of the upstream cylinder increases its complexity and becomes nonsymmetric with respect to the cylinder midspan. In addition, two recirculation zones appear in the wake of the downstream cylinder close to the end walls. Hence, the vortex shedding is not in phase along the span. For $Re = 200$, although the recirculation zones within the gap in the *X-Z* plane persist, the end effects lead to spanwise variation of shedding frequency along the span of the downstream cylinder. Note how the larger cells at the rear of the downstream cylinder promote an oblique mode of shedding, i.e., the shed cells are larger at the midspan region. Nonetheless, the stronger upward flow takes place close to the end walls. Fig. 19 shows how for $Ri = 3$ and both values of *Re*, strong upward flow is present within the gap and behind the downstream cylinder. However, the mean spanwise velocity field displays an irregular shedding pattern for $Re = 200$, indicating that a non-periodic vortex shedding pattern throughout the span is triggered by the strong opposing buoyancy.

4. Conclusions

The wakes between and downstream of a tandem arrangement of two isothermal circular cylinders of identical diameter confined inside a vertical channel have been investigated non-intrusively using the PIV technique. Experiments have been carried out for Reynolds numbers of $Re = 100$ and 200, fixed Prandtl number of $Pr = 7$, blockage ratio of $BR = D/H = 0.3$, aspect ratio of $AR = W/D = 5$, pitch-to-diameter ratio of $\sigma = 3$, and values of the buoyancy parameter (Richardson number) in the range $-1 \leq Ri \leq 3$. The results show that due to the mixed effects of wall proximity, buoyancy strength and mutual interference between the two cylinders, the Strouhal number and vortex shedding patterns are highly dependent on the combined values of *Re* and *Ri*. Based on the measured instantaneous and ensemble-averaged flow patterns, the main conclusions can be summarized as follows:

1. For both values of *Re* and assisting buoyancy ($Ri = -1$), the width of the wakes of both cylinders appears to narrow, vortex shedding is completely suppressed, and a stationary flow response is achieved.
2. For both values of *Re*, the separation angle is a decreasing function of *Ri* in the range $-1 \leq Ri \leq 3$. For $Re = 100$, the values of the separation angle of the downstream cylinder are up to 9.93% higher than those registered for the upstream one. However, the margin reduces to 1.62% for $Re = 200$.
3. For $Re = 100$, the Strouhal number increases for increasing values of the buoyancy parameter in the range $0 \leq Ri \leq 1$, it drops dramatically to $St \approx 0.12$ for $Ri = 2$, and the wake flow pattern becomes irregular for $Ri = 3$. For $Re = 200$, the Strouhal number is an increasing function of *Ri* in the range $0 \leq Ri \leq 2$, and depending on the value of buoyancy parameter, the flow behavior depicts periodic or quasi-periodic flow oscillation. For $Ri = 3$, a non-periodic wake pattern sets in.
4. For a fixed value of buoyancy strength, the vortex shedding patterns of both cylinders exhibit a strong dependence on *Re*. Parallel vortex shedding sets in for the unheated cylinders ($Ri = 0$). For $Ri = 1$, oblique and concave vortex shedding occurs for $Re = 100$ and $Re = 200$, respectively. For $Ri = 2$ and both values of *Re*, the end effects lead to spanwise variation of shedding frequency along the span of the downstream cylinder. Finally, for $Ri = 3$, the space within the gap and at the rear of the downstream cylinder is occupied by strong upward flow and the vortex shedding pattern is irregular.
5. The vortex shedding pattern of the cylinder array is significantly modified under varying thermal buoyancy, and buoyancy forces are tangibly more sensitive for the lower value of the Reynolds number studied.
6. A comparison between the experimental data and available two-dimensional numerical results for $Re = 100$ and 200 as a function of the Richardson number has been made. For values of the buoyancy parameter up to $Ri = 1$, good agreement has been found between the measured data and numerical simulations. However, for higher values of *Ri*, important differences in the flow motion appear, suggesting that the role of the three-dimensionality of the flow due to wall effects becomes very pronounced.

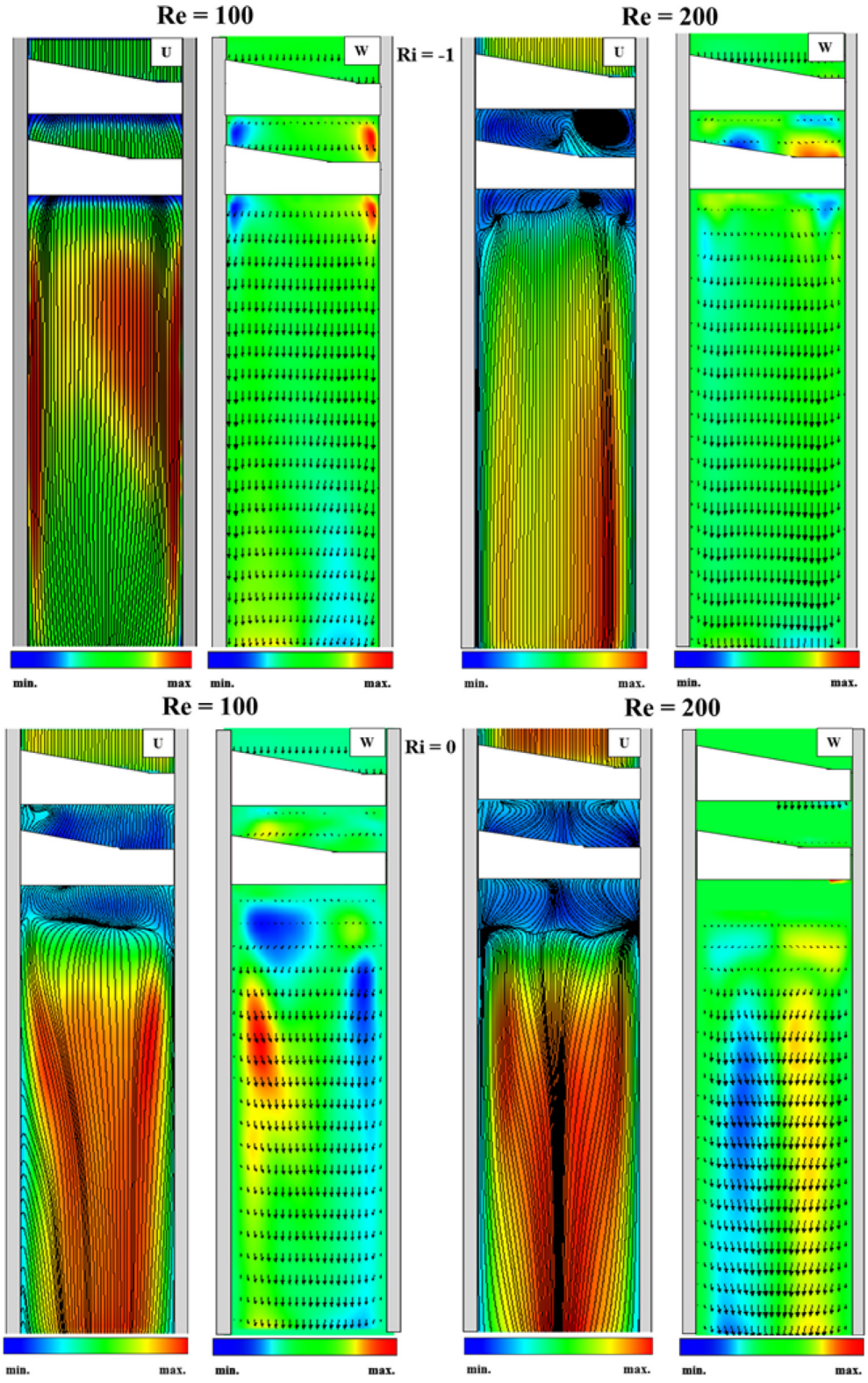

Fig. 17. Time-averaged flow pattern in the *X-Z* that goes through the cylinders' axes for $Ri = -1$ (top images) and $Ri = 0$ (bottom images) at $Re = 100$ and 200 (left and right), respectively. The images show from left to right the longitudinal and spanwise velocity fields, respectively.

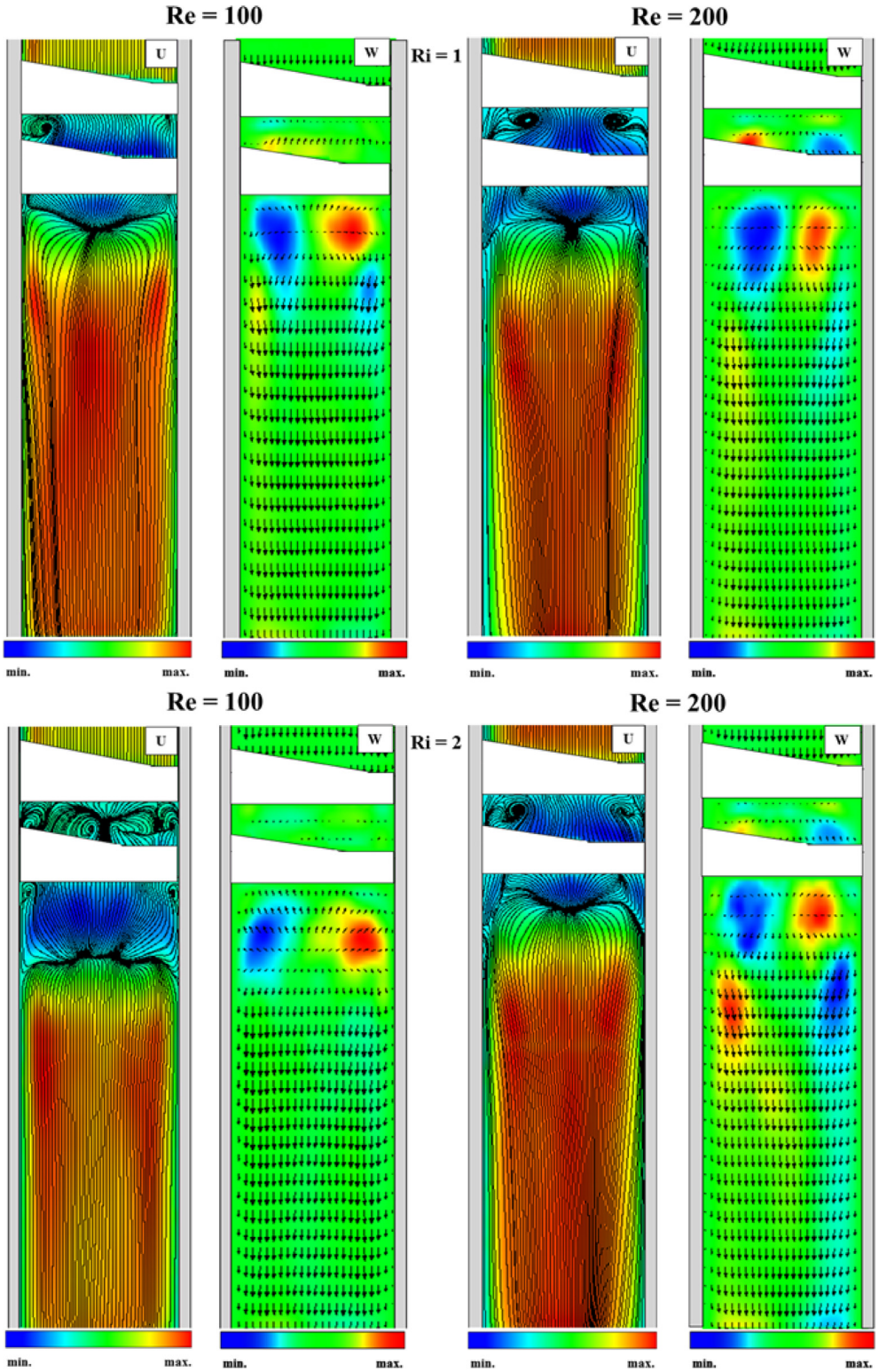

Fig. 18. Time-averaged flow pattern in the *X-Z* that goes through the cylinders' axes for $Ri = 1$ (top images) and $Ri = 2$ (bottom images) at $Re = 100$ and 200 (left and right), respectively. The images show from left to right the longitudinal and spanwise velocity fields, respectively.

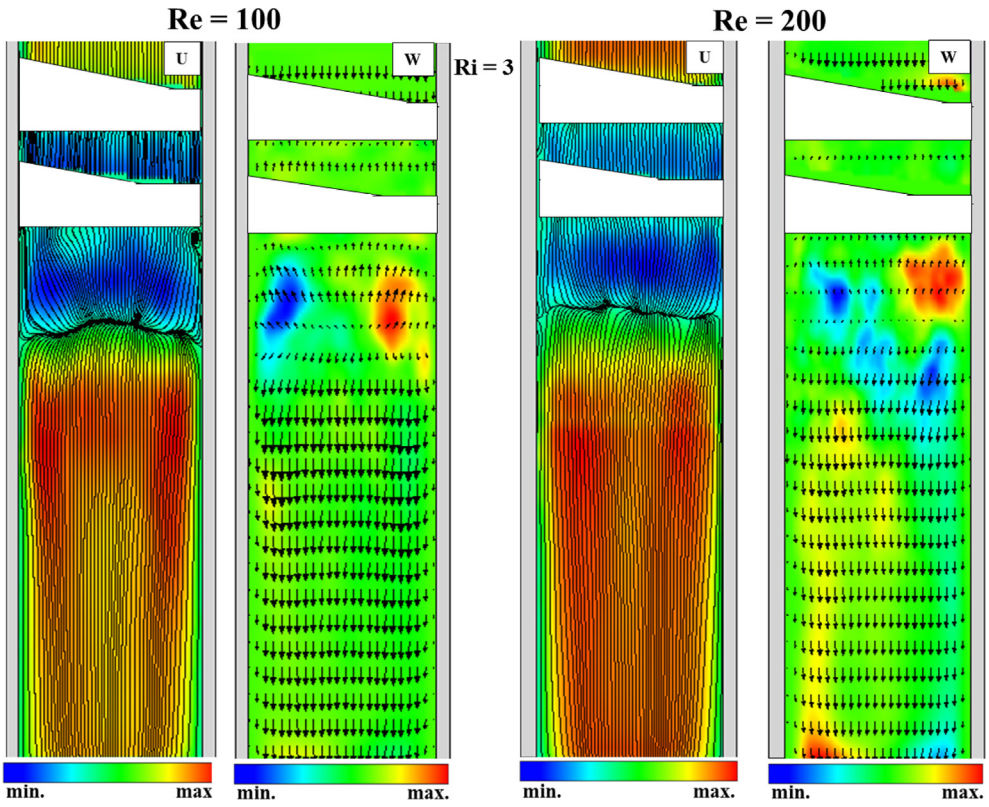

Fig. 19. Time-averaged flow pattern in the *X-Z* that goes through the cylinders' axes for $Ri = 3$ and $Re = 100$ and 200 (left and right), respectively. The images show from left to right the longitudinal and spanwise velocity fields, respectively.

Acknowledgments

This research was supported by the Consejo Nacional de Ciencia y Tecnología (CONACYT), Grant number 167474. The authors want to thank Faustino Pérez-Flores for his assistance in the experimental tests.

References

[1] Zdravkovich M. Flow around circular cylinders, vol. 1. USA: Oxford University Press; 1997.
[2] Zdravkovich M. Flow around circular cylinders, vol. 2. USA: Oxford University Press; 2003.
[3] Zdravkovich M. Review of flow interference between two circular cylinders in various arrangements. Trans ASME, J Fluids Eng 1977;99:618–33.
[4] Zdravkovich M. Flow induced oscillations of two interfering circular cylinders. J Sound Vib 1985;101:511–21.
[5] Zdravkovich M. The effects of interference between circular cylinders in cross flow. J Fluid Struct 1987;1:239–61.
[6] Sumner D. Two circular cylinders in cross-flow: a review. J Fluid Struct 2010;26:849–99.
[7] Sharman LDB, Lien FS, Norberg C. Numerical predictions of low Reynolds number flows over two tandem circular cylinders. Int J Numer Meth Fl 2004;47:423–47.
[8] Xu G, Zhou Y. Strouhal numbers in the wake of two inline cylinders. Exp Fluids 2004;37:248–56.
[9] Alam M, Zhou Y. Phase lag between vortex shedding from two tandem bluff bodies. J Fluid Struct 2007;23:339–47.
[10] Mussa L-SLA, Asinari P. Lattice Boltzmann simulations of 3D laminar flows past two tandem cylinders. J Comput Phys 2009;228:983–99.
[11] Hu H, Koochesfahani M. Thermal effects on the wake of a heated circular cylinder operating in mixed convection regime. J Fluid Mech 2011;685:235–70.
[12] Igarashi T. Characteristics of the flow around two circular cylinders arranged in tandem. 1st Rep JSME B 1981;24:323–31.
[13] Igarashi T. Characteristics of the flow around two circular cylinders arranged in tandem. 2nd Rep JSME 1984;27:2380–7.
[14] Meneghini J, Saltara F, Siqueira C, Ferrari Jr J. Numerical simulation of flow interference between two circular cylinders in tandem and side-by-side arrangements. J Fluid Struct 2001;15:327–50.
[15] Lin J, Yang Y, Rockwell D. Flow past two cylinders in tandem: instantaneous and averaged flow structure. J Fluid Struct 2002;16:1050–71.
[16] Hiwada IMM, Yanagihara H. Fluid flow and heat transfer around two circular cylinders in cross flow. Bull JSME 1982;25:1737–45.
[17] Hetz MDAA, Telionis D. Vortex shedding over five in-line cylinders. J Fluid Struct 1991;5:243–57.
[18] Lee T, Basu S. Nonintrusive measurements of the boundary layer developing on a single and two circular cylinders. Exp Fluids 1997;23:187–92.
[19] Ljungkrona L, Norberg C, Sundén B. Free-stream turbulence and tube spacing effects on surface pressure fluctuations for two tubes in an in-line arrangement. J Fluid Structr 1991;5:701–27.
[20] Ljungkrona L, Sundén B. Flow visualization and surface pressure measurement on two tubes in an inline arrangement. Exp Therm Fluid Sci 1993;6:15–27.
[21] Ishigai S, Nishikawa E, Nishimura K, Cho K. Experimental study of structure of gas flow in tube banks with tube axes normal to flow (part 1, kármán vortex flow from two tubes at various spacings. JSME 1972;15:949–56.
[22] Alam M, Meyer J. Two interacting cylinders in cross flow. Phys Rev E 2011;84:056304.
[23] Li J, Chambarel A, Donneaud M, Martin R. Numerical study of laminar flow past one and two circular cylinders. Comput Fluids 1991;19:155–70.
[24] Johnson A, Tezduyar T, Liou J. Numerical simulation of flows past periodic arrays of cylinders. Comput Mech 1993;11:371–83.
[25] Ding H, Shu C, Yeo K, Xu D. Numerical simulation of flows around two circular cylinders by mesh-free least square-based finite difference methods. Int J Numer Meth Fluids 2007;53:305–32.
[26] Singha S, Sinhamahapatra K. High-resolution numerical simulation of the flow about two cylinders in tandem at low Reynolds numbers. ASME J Fluids Eng 2010;132:1–10.
[27] Jiang R, Lin J, Chen Z. Vibrations of cylindrical objects obstructing a Poiseuille-type flow. Phys Rev E 2013;88:023009.
[28] Jiang R-J, Lin J-Z, Ku X-K. Flow-induced vibrations of two tandem circular cylinders in a parallel-wall channel. Phys Fluids 2014;26:104102.
[29] Nejat A, Abdollahi V, Vahidkhah K. Lattice Boltzmann simulation of non-Newtonian flows past confined cylinders. J Newt Fluid Mech 2011;166:689–97.
[30] Lin J, Jiang R, Chen Z, Ku X. Poiseuille flow-induced vibrations of two cylinders in tandem. J Fluid Struct 2013;40:70–85.
[31] Shyam R, Sasmal C, Chhabra R. Natural convection heat transfer from two vertically aligned circular cylinders in power-law fluids. Int J Heat Mass Transf 2013;64:1127–52.

[32] Chouikh R, Guizani A, Maâlej, Belghith A. Numerical study on the laminar natural convection flow around an array of two horizontal isothermal cylinders. Int Commun Heat Mass Transf 1999;26:329–38.
[33] Chouikh R, Guizani A, Cafsi E, Maâlej M, Belghith A. Experimental study of the natural convection flow around an array of heated horizontal cylinders. Renew Energy 2000;21:65–78.
[34] Corcione M. Correlating equations for free convection heat transfer from horizontal isothermal cylinders set in a vertical array. Int J Heat Mass Transf 2005;48:3660–73.
[35] Paykoc HYE, Bezzazoğlu M. Laminar natural convective heat transfer over two vertically spaced isothermal horizontal cylinders. Exp Therm Fluid Sci 1991;4:362–8.
[36] Sadeghipour M, Asheghi M. Free convection heat transfer from arrays of vertically separated horizontal cylinders at low Rayleigh numbers. Int J Heat Mass Transf 1994;37:103–9.
[37] Sparrow E, Niethammer J. Effect of vertical separation distance and cylinder-to-cylinder temperature imbalance on natural convection for a pair of horizontal cylinders. J Heat Transf 1981;103:638–44.
[38] Tokura I, Saito H, Kishinami K, Muramoto K. An experimental study of free convection heat transfer from a horizontal cylinder in a vertical array set in free space between parallel walls. J Heat Transf 1983;105:102–7.
[39] Peersons T, O'Gorman I, Donoghue D, Byrne G, Murray D. Natural convection heat transfer and fluid dynamics of a pair of vertically aligned isothermal horizontal cylinders. Int J Heat Mass Transf 2011;54:5163–72.
[40] Ashjaee M, Yousefi T, Farahmand S, Chavoshi E. Enhancement of free convection heat transfer from a vertical array of isothermal cylinders by flow diverters. Heat Transf Eng 2009;30:197–206.
[41] Ashjaee M, Yousefi T. Experimental study of free convection heat transfer from horizontal isothermal cylinders arranged in vertical and inclined arrays. Heat Transf Eng 2007;28:460–71.
[42] Chae M, Chung B. Effect of pitch-to-diameter ratio on the natural convection heat transfer of two vertically aligned horizontal cylinders. Chem Eng Sci 2011;66:5321–9.
[43] D'Orazio A, Fontana L. Experimental study of free convection from a pair of vertical arrays of horizontal cylinders at very low Rayleigh numbers. Int J Heat Mass Transf 2010;53:3131–42.
[44] Bejan A, Fowler A, Stanescu G. The optimal spacing between horzontal cylinders in a fixed volume cooled by natural convection. Int J Heat Mass Transf 1995;38:2047–55.
[45] Park S, Chang K. Numerical study on interactive laminar natural convection from a pair of vertically separated horizontal cylinders. Numer Heat Transf 1988;14:61–74.
[46] Zhang Y, Chen Z. Effect of gap between layers on the heat transfer performance of aligned tube banks. Heat Transf Eng 1992;13:33–41.
[47] Zukauskas A. Heat transfer from tubes in cross flow. Adv Heat Transf 1972;8:93–160.
[48] Zhou Y, Yiu M. Flow structure, momentum and heat transport in a two-tandem-cylinder wake. Exp Fluids 2006;548:17–48.
[49] Gori F, Petracci I, Tedesco V. Cooling of two smooth cylinders in row by a slot jet of air with low turbulence. Appl Therm Eng 2007;27:2415–25.
[50] Jiang R-J, Lin J-Z. Wall effects on flows past two tandem cylinders of different diameters. J Hydrodyn 2012;24:1–10.
[51] Harimi I, Saghafian M. Numerical simulation of fluid flow and forced convection heat transfer from tandem circular cylinders using overset grid method. J Fluid Struct 2012;28:309–27.
[52] Gowda YK, Patnaik B, Narayana PA, Seetharamu K. Finite element simulation of transient laminar flow and heat transfer past an in-line tube bank. Int J Heat Fluid Fl 1998;19:49–55.
[53] Chen C, Wang T-S. Finite analytic solution of convective heat transfer for tube arrays in cross flow: Part ii - heat transfer analysis. ASME J Heat Transf 1989;111:641–8.
[54] Mahir N, Altaç Z. Numerical investigation of convective heat transfer in unsteady flow past two cylinders in tandem arrangements. Int J Heat Fluid Fl 2008;29:1309–18.
[55] Juncu G. A numerical study of momentum and forced convection heat transfer around two tandem circular cylinders at low Reynolds numbers. Part I: momentum transfer. Int J Heat Mass Tran 2007a;50:3788–98.
[56] Juncu G. A numerical study of momentum and forced convection heat transfer around two tandem circular cylinders at low Reynolds numbers. Part II: forced convection heat transfer. Int J Heat Mass Tran 2007b;50:3799–808.
[57] Patnaik B, Narayana P, Seetharamu K. Finite element simulation of transient laminar flow past a circular cylinder and two cylinders in tandem. Int J Numer Method H 2000;10:560–80.
[58] Salcedo E, Cajas J, Treviño C, Martínez-Suástegui L. Unsteady mixed convection heat transfer from two confined isothermal circular cylinders in tandem: buoyancy and tube spacing effects. Int J Heat Fluid Flow 2016a;60:12–30.
[59] Salcedo E, Cajas J, Treviño C, Martínez-Suástegui L. Numerical investigation of mixed convection heat transfer from two isothermal circular cylinders in tandem arrangement: buoyancy, spacing ratio and confinement effects. Theor Comp Fluid Dyn 2016. http://dx.doi.org/10.1007/s00162–016–0411–z.
[60] Dumouchel F, Lecordier J, Paranthoen P. The effective Reynolds number of a heated cylinder. Int J Heat Mass Tran 1998;41:1787–94.
[61] Hatton A, James D, Swire H. Combined forced and natural convection with low-speed air flow over horizontal cylinders. J Fluid Mech 1970;42:17–31.
[62] Wang A-B, Travnicek Z, Chia K-C. On the relationship of effective Reynolds number and Strouhal number for laminar vortex shedding of a heated circular cylinder. Phys Fluids 2000;12:1401–10.
[63] Guillén I, Treviño C, Martínez-Suástegui L. Unsteady laminar mixed convection heat transfer from a horizontal isothermal cylinder in contra-flow: buoyancy and wall proximity effects on the flow response and wake structure. Exp Therm Fluid Sci 2014;52:30–46.
[64] Brika D, Laneville A. Vortex-induced vibrations of a long flexible circular cylinder. J Fluid Mech 1993;250:481–508.
[65] Brika D, Laneville A. An experimental study of the aeolian vibrations of a flexible circular cylinder at different incidences. J Fluid Struct 1995;9:371–91.
[66] Khalak A, Williamson C. Motions, forces and mode transitions in vortex-induced vibrations at low mass-damping. J Fluid Struct 1999;13:813–51.
[67] Sarpkaya T. A critical review of the intrinsic nature of vortex- induced vibrations. J Fluid Struct 2004;19:389–447.
[68] Singh S, Mittal S. Vortex-induced oscillations at low Reynolds numbers: hysteresis and vortex-shedding modes. J Fluid Struct 2005;20:1085–104.
[69] Shiels D, Leonard A, Roshko A. Flow-induced vibration of a circular cylinder at limiting structural parameters. J Fluid Struct 2005;20:1085–104.
[70] Newman D, Karniadakis G. Direct numerical simulations of flow over a flexible cable. In: Bearman PW, editor. Proc. Sixth int. Conf. On flow-induced vibration. Rotterdam: Balkema; 1995.
[71] Wang L, Hou K, Lu J, Hsu C. Flow patterns of mixed convection in a horizontal square channel flow. Exp Heat Transf 1996;9:257–65.
[72] Kline S, McClintock F. Describing uncertainty in single sample experiments. Mech Eng 1953;75:3–12.